Master Thesis in Geographical Information Science nr 112

Aspects of Error Quantification and Evaluation in Digital Elevation Models for Glacier Surfaces

Jip J. van Zoonen

2020

Department of
Physical Geography and Ecosystem Science
Centre for Geographical Information Systems
Lund University
Sölvegatan 12
S-223 62 Lund
Sweden

Jip J. van Zoonen (2020). Aspects of Error Quantification and Evaluation in Digital Elevation Models for Glacier Surfaces.
Master degree thesis, 30 credits in Master in Geographical Information Science
Department of Physical Geography and Ecosystem Science, Lund University

Aspects of Error Quantification and Evaluation in Digital Elevation Models for Glacier Surfaces

---

Jip Jan van Zoonen
Master thesis, 30 credits, in Geographical Information Sciences

Supervisor
Abdulghani Hasan
Lund University

ABSTRACT

This study explores methods to quantify and evaluate error in digital elevation models (DEMs) built from remotely sensed elevation data of the Hintereisferner glacier. A special focus lies on glacier surfaces because glaciers are often inaccessible for field observations but at the same time prone to measurement errors. They would therefore particularly benefit from a comprehensive error assessment.

One of the primary aspects of the study is to find suitable methods that also include the spatial distribution of error because this is generally a somewhat neglected aspect of quality assessment of DEMs, although it has a potentially significant impact on the way DEMs are used in research. Especially if geomorphological or topographical aspects are part of this. In addition to identifying and discussing methods to quantify and evaluate existing errors in DEMs, this study also looks at some of the major sources from which the errors stem to find out if the influence of these sources on the resulting errors can be estimated. To this end, two out of three major categories of error sources were selected: interpolation effects and spatial resolution effects.

The explored methods include quantitative error measures, such as RMSE, but also more evaluative approaches, such as correlation analysis. Including spatial distribution as part of the quantification and evaluation of error in DEMs is done by exploring methods like the creation of error surfaces or approaches that quantify the spatial patterning of error values in DEMs, such as Moran's I.

The results show that when it comes to quantification and evaluation of error in DEMs, error surfaces, in combination with a mapped overview of the Local Moran's I values, are presumably the most powerful methods to gain insight into both the absolute error values and the spatial distribution of them. Particularly spatial outlier detection is a useful part of this approach.

TABLE OF CONTENTS

ABSTRACT…….. iv
TABLE OF CONTENTS v
LIST OF ACRONYMS AND ABBREVIATIONS vii
LIST OF TABLES AND FIGURES viii
1. INTRODUCTION 1
1.1 The importance of remote sensing for topographic analysis in glaciology 1
1.2 Quality of remotely sensed topographic data 2
1.3 Research motivation 3
1.4 Research objectives 3
1.5 Thesis outline 5
2. THEORETICAL BACKGROUND 7
2.1 Imaging radar 7
2.2 Interferometric synthetic aperture radar (InSAR) 8
2.3 Photogrammetry and stereo image data 10
2.4 Light detection and ranging (LiDAR) 12
2.5 Digital elevation models (DEMs) 14
2.5.1 The use of DEMs in glaciology 15
2.6 Quality assessment of DEMs 16
2.6.1 Spatial accuracy 17
2.6.2 Interpolation methods 17
2.6.3 Scale effects and spatial resolution 19
3. DATA AND METHODS 21
3.1 Study area: Hintereisferner 21
3.2 Remote sensing data 23
3.2.1 ASTER GDEM 24
3.2.2 LiDAR 24
3.3 Data preparation 25
3.4 Compilation of derived topographic parameters 26
3.4.1 Slope 26
3.5 Error quantification and evaluation 29
3.5.1 Quantifying and evaluating interpolation effects 34
3.5.2 Quantifying and evaluating spatial resolution effects 35
4. RESULTS AND DISCUSSION 37

4.1 Overview of the processed elevation data and descriptive statistics 37
4.1.1 RMSE 40
4.2 Correlation analysis 42
4.3 Error Surfaces 45
4.4 Measures of spatial autocorrelation and clustering 48
4.4.1 Global Moran's I 48
4.4.2 Getis-Ord General G 49
4.4.3 Local Moran's I 50
4.4.4 Getis-Ord Gi* 51
4.5 Quantifying and evaluating major sources of error in DEMs 53
4.5.1 Interpolation effects 53
4.5.2 Spatial resolution effects 55
4.6 Caveats and limitations 58
5. CONCLUSIONS AND RECOMMENDATIONS 59
REFERENCES 65
Series from Lund University 77

LIST OF ACRONYMS AND ABBREVIATIONS

ALS: Airborne Laser Scanning

ASTER: Advanced Spaceborne Thermal Emission and Reflection Radiometer

DEM: Digital Elevation Model

ETRS89: European Terrestrial Reference System 1989

GDEM: Global Digital Elevation Map

GNSS: Global Navigation Satellite System

GPS: Global Positioning System

ICESat: Ice, Cloud, and land Elevation Satellite

IDW: Inverse Distance Weighting

IMU: Inertial navigational Measurement Unit

InSAR: Interferometric Synthetic Aperture Radar

LAS: LASer file format

LiDAR: Light Detection and Ranging

LISA: Local Indicators of Spatial Association

METI: Ministry of Economy, Trade and Industry (Japan)

NASA: National Aeronautics and Space Administration

SAR: Synthetic Aperture Radar

SRTM: Shuttle Radar Topography Mission

TIN: Triangulated Irregular Network

UTM: Universal Transverse Mercator

LIST OF TABLES AND FIGURES

Table 1. Specifications of the ASTER GDEM dataset used in this study.
Table 2. Specifications of the LiDAR dataset used in this study.
Table 3. Data specifications of the different DEMs after data preparation.
Table 4. Error quantification for the topographic parameter elevation, based on RMSE.
Table 5. Descriptive statistics for the values of the elevation error surface.
Table 6. Global Moran's I index as a measure for spatial autocorrelation and clustering in the study area.
Table 7. Getis-Ord General G as a measure for spatial autocorrelation and clustering in the study area.
Table 8. Error quantification for the interpolated DEM.

Figure 1. SAR interferometric configuration for the estimation of surface elevation.
Figure 2. Configuration of the stereo-imaging capability of the ASTER sensor, onboard the Terra satellite.
Figure 3. ALS configuration.
Figure 4. Typical DEM data structures.
Figure 5. Example of segmentation results as spatial resolution is altered.
Figure 6a. Overview of the European Alps with the approximate location of the Hintereisferner glacier.
Figure 6b. Part of the Austrian Alps where the Hintereisferner glacier is located.
Figure 6c. Spatial extent of the study area.
Figure 7. The values of the center cell and its eight neighbors determine the horizontal and vertical gradients.
Figure 8. Overview of the ASTER GDEM elevation data for the Hintereisferner.
Figure 9. Overview of the high-resolution LiDAR-based reference elevation data for the Hintereisferner.
Figure 10. Frequency distribution and descriptive statistics for the low-resolution ASTER GDEM elevation data.
Figure 11. Frequency distribution and descriptive statistics for the high-resolution LiDAR reference data.

Figure 12. The Hintereisferner glacier with two different sample areas to illustrate how a single RMSE value disregards spatial heterogeneity.
Figure 13. Sample grid with 3034 sample points and 50 m interval to extract elevation values to compare for correlation analysis.
Figure 14a. Correlation analysis for ASTER GDEM DEM versus the LiDAR reference DEM.
Figure 14b. Correlation analysis for ASTER GDEM DEM versus the LiDAR reference DEM for a small part of the study area with relatively low elevation levels (sample 2 in Figure 12).
Figure 15. The error surface is constructed by calculating the differences between the elevation values of the ASTER GDEM elevation model and the ones from the LiDAR reference elevation model.
Figure 16. Frequency distribution of the error values based on the ones that are depicted in Figure 15.
Figure 17. Absolute elevation differences (i.e. error values) that result from comparison of the ASTER GDEM DEM with the LiDAR reference DEM.
Figure 18. Cluster and outlier detection based on Local Moran's I.
Figure 19. Error hot spot and cold spot analysis based on the Getis-Ord Gi* statistic.
Figure 20. Map of the filtered error hot spot analysis.
Figure 21. An overview of the interpolated ASTER GDEM DEM of the Hintereisferner glacier.
Figure 22. Level of agreement between the interpolated DEM and the LiDAR reference DEM.
Figure 23. Mapped slope values for the LiDAR reference data.
Figure 24. Comparison of slope values against elevation differences (i.e. error values) for the whole study area.
Figure 25. Level of agreement between the error values and slope values to determine the influence of spatial resolution effects.

1. INTRODUCTION

With the introduction of satellite-based observation techniques in the second half of the 20th century, topographic analysis made a significant leap forward. Not only do the remotely sensed data enable easy digital mapping on a global or regional scale, they also offer many possibilities to analyze both global and local shape and features of the Earth's surface, much to the benefit of geosciences in general. Considering the current increasing awareness of global changes in our planet's natural cycles and processes, remote sensing is one of the strongest tools imaginable for monitoring these changes from a topographical perspective.

Remote sensing technologies (e.g. spectral imaging, such as Synthetic Aperture Radar (SAR)) provide data that can be used to analyze all sorts of topographic objects, including glaciers and glacial landforms. Because of the wide recognition of glaciers as indicators for climate change, studying them with the aid of remote sensing technologies has become an expanding field of research over the past decades.

1.1 The importance of remote sensing for topographic analysis in glaciology

Remote sensing of glaciers plays a fundamental role in our understanding of their characteristics and dynamics, not least because the remoteness of glaciers and difficulty to gain access for in-situ measurements mean that remote sensing data is, in some cases, an absolute necessity. Many of the glaciological applications of remote sensing are concerned with shape, relief and deformation of glaciers. Glaciological features that are extensively studied and monitored with remote sensing techniques include geometry (e.g. area, outline, surface roughness or thickness), mass balance (proxies), flow/surge velocity, surface albedo, snow-line retreat, elevation change, etc. (e.g. Gao & Liu, 2001; Bamber & Rivera, 2007; Li et al., 2011; Nuth & Kääb, 2011; Scherler et al., 2011; Gärtner-Roer et al., 2014; Kääb et al., 2016; Naegeli et al., 2017).

Virtually all of these features are related to the topography of the glacier. For example, research that studies the width, length and slope influences on glacier surging shows that normal and surge-type glaciers have significantly different average geometries. Surge-type glaciers tend to be longer, wider and to have lower overall slope than normal glaciers, and there seems to be a fundamental correlation between length and surge tendency

(Kamb, 1987; Clarke, 1991). To support these findings the topography of glaciers as well as flow rates can be accurately measured by remote sensing devices. More recent studies that involve remotely sensed measurements of glacier geometry include research that was conducted by Felikson et al. (2017) on the inland thinning of the Greenland ice sheet, which shows that the up-glacier extent of thinning and, thus, mass loss, is limited by glacier geometry, or the research that was done by Sevestre & Benn (2015) which investigates correlations between the distribution of surge-type glaciers and climatic and glacier geometry variables.

Another example within the field of glaciology where remote sensing techniques are increasingly put to use is the study of energy and mass balances, which is often related to the three-dimensional geometry of the glacier but can be based on surface topography as well. Arnold et al. (2006a), for example, investigated the role played by topography on the spatial distribution of energy balance components, and hence melt. Their study found that topography plays a vital role in explaining the spatial complexity when modelling energy fluxes. This is mainly because incoming solar radiation is strongly affected by the topography of the glacier surface itself, e.g. through the interactions between solar geometry and the surface slope and aspect, which determines the incident angle of direct solar radiation, but also because the topography of the surrounding terrain controls shading patterns over the glacier (affecting direct solar radiation) and influences the amount of diffuse radiation that is received by the glacier. In their conclusion, Arnold et al. point out that, although in-situ stake measurements will continue to be an important tool in mass balance monitoring, the results from their research show that the process of monitoring mass balance benefits enormously from remotely sensed topographic data. A point of view that is widely acknowledged among scientists in this field (e.g. Bamber & Rivera, 2007; Rivera et al., 2007; Joerg et al, 2012; Schellenberger et al., 2016; Goerlich et al., 2017; Neelmeijer et al., 2017; Rabatel et al., 2017).

1.2 Quality of remotely sensed topographic data

The aforementioned examples show that remote sensing techniques are indispensable when it comes to topographic analysis of glaciers. There is, however, often a rather large variation in quality with regard to satellite-based remotely sensed data. This, of course, differs from case to case and depends to a large extent on the application and the specific data requirements, but it is also due to things like measurement accuracy, data processing,

and systematic biases. It is therefore important to validate and compare the quality of topographic data sources and one of the more obvious ways to do this is by looking at elevation errors in the data.

Topographic analysis of glaciers is often based on the use of a digital elevation model (DEM). In light of the importance of precise and accurate remotely sensed data for these analyses, the user of a DEM would most certainly benefit from a comprehensive error quantification and evaluation because, as Gonga-Saholiariliva et al. (2011) point out, knowledge on the scope of error and where these errors are located determines how to correct DEMs to minimize error accumulation or how to include these factors in the interpretation of DEM-based research.

1.3 Research motivation

As mentioned earlier in this introduction, glaciers are often located in inaccessible or remote places. On top of that, remote sensing of glaciers presents a broad range of challenges (Racoviteanu et al., 2009), including measurement difficulties with regard to topographic parameters. With SAR interferometry, for instance, there is often a certain bias to the measurements that is caused by the penetration depth (Rignot et al., 2001; Dall, 2007; Abdullahi et al., 2018). Gaining a complete picture of the error in digital elevation models for glacier surfaces, including its spatial distribution, is therefore highly beneficial to researchers in the field. Any additional glaciological field surveys, for instance, can be conducted in a much more efficient way by reducing it to targeted observations, based on the outcomes of the error quantification and evaluation, which will eventually result in a more adequate elevation model of the glacier.

1.4 Research objectives

A significant amount of research has been carried out that has accuracy assessment of DEMs as its primary focus. Also, some attempts to model the spatial distribution of error in DEMs can be found in the literature (see, for example, Carlisle (2005)). This study, however, explores several methods of error quantification and evaluation, including the spatial component of error distribution, to offer more insight into the suitability of these methods, specifically for glacier surfaces.

Errors in DEMs can be quantified and evaluated by comparing the elevation data - or other corresponding topographic parameters - to high-resolution reference data that function as (an approximation of) 'ground truth', because, by doing so, the accuracy of the DEM is tested through relating this to the best approximation of what is considered as actual elevation values. (Wechsler & Kroll, 2006; Vaze et al., 2010; Purinton & Bookhagen, 2017). It is important to mention, though, that reference data as such is acquired and processed in ways that are comparable to the data acquisition from the coarser DEM, albeit with higher precision and accuracy.

To provide a comprehensive overview of suitable methods for error quantification and evaluation in DEMs, some commonly used measures of accuracy, such as Root Mean Square Error (RMSE), are complemented by an analysis of the spatial distribution of error, e.g. through error surfaces and measures of spatial autocorrelation. As Wechsler & Kroll (2006) point out, error values such as the RMSE ignore the spatial structure of error, which can be problematic because elevation tends to be spatially autocorrelated – and therefore DEM error often as well.

In addition to the methods that quantify and evaluate actual error values in DEMs, there are also methods that rather look at the sources where the errors stem from. The main sources of error in DEMs fall into three categories:

- those derived from variations in the accuracy, density, and distribution of the measured source data and possible (systematic) biases during data acquisition,
- those derived from data processing and interpolation, and
- those resulting from the characteristics of the land surface, which are often linked to the spatial resolution (Fisher & Tate, 2006). The importance of spatial resolution effects in glaciological research, for instance, is clearly shown in the mass balance studies by Arnold et al. (2006a) and Rees & Arnold (2006).

The first category of error sources – in short: measurement errors - is rather difficult to quantify or evaluate because this is typically a matter of validation or calibration of the remote sensing device. This aspect is ignored in this study because it generally does not fall within the scope of the explored methods. However, the other two categories – interpolation effects and spatial resolution effects – are included in this study because they are quantified and evaluated in similar ways as the original errors.

Interpolation effects can be evaluated by comparing error values of the interpolated DEM against the error values of the DEM on which the interpolation was applied. Quantifying and evaluating spatial resolution effects require a more sophisticated approach. Here, a derived topographic parameter – slope – is compiled to serve as a proxy for spatial resolution effects. This relationship is derived from the literature. Several studies have shown that derived topographic parameters are often inconsistent when the spatial resolution of the DEM is changed (Chen & Zhou, 2013), and error in these parameters is positively related to the spatial resolution of the DEM (Chang & Tsai, 1991).

In view of the foregoing, the general aim of this study is to explore and discuss suitable methods that can be used to quantify and evaluate error, the spatial distribution of error, and the sources of error in digital elevation models for glacier surfaces.

1.5 Thesis outline

Chapter 2 starts with some background information on the various remote sensing techniques that are used in this study and continues with an explanation of the different types of quality assessment of DEMs, including error quantification. Chapter 3 gives a brief description of the study area. In chapter 4, the data and methods that are used in this study are described. In chapter 5, results are displayed, interpreted and discussed. Finally, conclusions are drawn in chapter 6.

2. THEORETICAL BACKGROUND

There are numerous remote sensing-based methods for obtaining elevation data, which, in turn, are used to create DEMs. The publicly available DEMs from the Shuttle Radar Topography Mission (SRTM), for instance, are derived from spaceborne interferometric synthetic aperture radar (InSAR). Due to their wide, almost global spatial coverage, these DEMs are often used in geoscientific research, e.g. in glacial mass balance studies (Gardelle et al., 2012). Another popular source of elevation data in geoscientific research – glaciology in particular – is the Ice, Cloud, and Land Elevation Satellite (ICESat) mission, which acquired its elevation data via a method that makes use of laser scanning. This thesis primarily focuses on two remote sensing-based methods for the creation of DEMs: photogrammetry (more specifically optical stereo data pairing) and a specific form of laser scanning called Light Detection and Ranging (LiDAR).

The basic concepts of imaging radar, interferometry, photogrammetry, LiDAR, and the creation of DEMs will be explained in this chapter. For a detailed description of imaging radars and an in-depth explanation of radar interferometry, the reader is referred to Hanssen (2001). Kääb (2010) provides extensive information on photogrammetry with a particular focus on glacier studies. For an in-depth introduction to theories and principles of LiDAR technology, Shan & Toth (2008) are an informative source. A comprehensive overview of the major applications of LiDAR is provided by Vosselman & Maas (2010).

2.1 Imaging radar

Typical radar systems measure the strength and round-trip time of the electromagnetic waves in the radio or microwaves domain that are emitted by a radar antenna and reflected off a distant surface or object. The radar antenna alternately transmits and receives pulses at particular wavelengths and polarizations. The receiver and processor then determine the properties of the distant surface or object, e.g. location or speed.

For an imaging radar system, over a thousand high-power pulses per second are transmitted toward the target or imaging area, with each pulse having a pulse duration of typically 10 to 50 microseconds. The pulse normally covers a small band of frequencies (Richards, 2009). At the Earth's surface, the energy in the radar pulse is scattered in all directions, with some reflected back toward the antenna. This backscatter returns to the

radar as a weaker signal and is received by the antenna. These signals are then converted to digital data and processed to display as an image.

A specific form of imaging radar that is widely used in remote sensing and mapping of the surface of the Earth is Synthetic Aperture Radar (SAR). SAR is an imaging radar device that is typically mounted on a moving platform, such as an aircraft or satellite. Similar to conventional radar, electromagnetic waves are sequentially transmitted, and the radar antenna collects the backscattered echo signals. However, SAR uses the motion of the radar antenna over a target region to provide finer spatial resolution than conventional radars. This technique synthesizes a very large antenna aperture by combining echo signals received by the radar as it moves along its flight track (Moreira et al., 2013). Typically, the larger the aperture, the higher the image resolution will be. This is regardless of whether the aperture is physical (a large antenna) or synthetic (a moving antenna), thereby allowing SAR devices to create high-resolution images with relatively small physical antennas.

2.2 Interferometric synthetic aperture radar (InSAR)

The basic design of a SAR system can be enhanced to collect more information. Most of these methods use the same basic principle of combining many pulses to form a synthetic aperture but may involve additional antennas or significant additional processing. Because of the coherent imaging technique used in SAR, the radiometric phase and amplitude are preserved during measurements. Rather than discarding the phase data, information can be extracted from it (Burgmann et al., 2000). If two observations of the same terrain from very similar positions are available, aperture synthesis can be performed. This aperture synthesis is a type of interferometric SAR and uses two or more SAR images to generate maps of surface deformation or elevation, using differences in the phase of the waves of the echo signals that are returned to the SAR devices (see Figure 1).

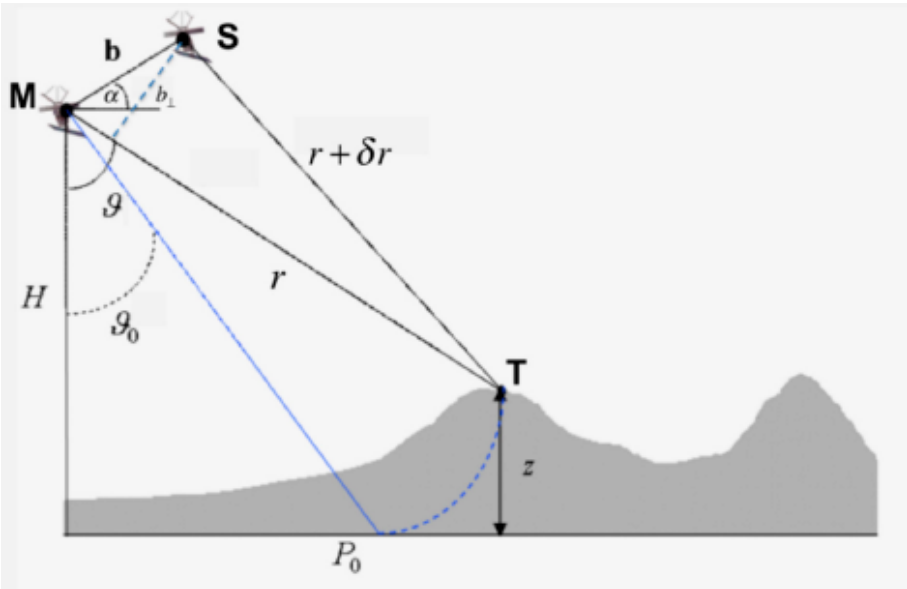

Figure 1. *SAR interferometric configuration for the estimation of surface elevation. M represents the orbital position where the master image is captured and S the orbital position where the slave image is captured. The interferometric phase map (called an interferogram) is formed on a pixel-by-pixel basis, starting from the two master and slave SAR images (Pepe & Calò, 2017).*

In order for aperture synthesis to work, the SAR devices are either in a closely controlled twin constellation (e.g. the TanDEM-X mission (Rizzoli et al., 2012)), are equipped with two antennas on the same moving platform some distance apart or revisit each area after a certain amount of time while observing from a slightly different incidence angle. The twin configuration or revisiting practice ensures the interferometric configuration of the sensor allowing for radiometric calculations. The difference in radiometric phase between two acquisitions can ultimately be related to topographic characteristics such as surface elevation (Ferretti et al., 2007).

An important advantage of obtaining the two sample signals simultaneously, e.g. with satellite systems in twin constellation, is that in this case any phase difference that contains information about the angle from which the radar echo returned, can be processed at the spot. Combining these phase differences with the distance information, one can determine the position in three dimensions of the image pixel. In other words, one can extract surface elevation as well as radar reflectivity and instantly produce a DEM.

If the two samples are separated in time, e.g. from two orbits over the same terrain, then there are two possible sources of phase shift. The first is surface elevation, as discussed above. The second is terrain motion. If the terrain has shifted between observations, it will return a different phase. The amount of shift required to cause a significant phase difference is in the order of the wavelength used. This means that if the terrain shifts by centimetres, it can be seen in the resulting image (a DEM must be available to separate the two kinds of phase difference). This second method also offers a powerful tool in geosciences. Glacier flow, for example, can be mapped with two passes of the moving platform (Pepe & Calò, 2017).

2.3 Photogrammetry and stereo image data

In essence, photogrammetry can be seen as a technique to obtain spatial measurements of objects depicted on images, such as photographs. This technique is applied in a broad variety of disciplines, most notably engineering, but in the case of geoscientific research it is commonly used as a rather efficient way of (digitally) mapping the topography of large and inaccessible areas, e.g. by making use of aerial photographs. The measurements that are used in topographic mapping are typical of a spatial nature and include aspects like the distances between features in an area of interest or areal extent. As Kääb (2010) points out, it is the capability to obtain quantitative spatial information over large areas without requiring direct ground access that led to the early application of photogrammetry in glaciology, where the technique is mostly used for mapping glacier surface features or measurement of surface displacements and the generation of DEMs. In recent decades, the use of photogrammetric methods has seen a shift from analogue aerial photography towards digital imagery from both airborne and spaceborne sensors (Khorram et al., 2012).

Basic applications of photogrammetry are bounded to the horizontal plane, with only two dimensions available. For the generation of DEMs, however, additional spatial information is needed to adequately estimate the three-dimensional coordinates of a point. To be able to do this, a more comprehensive form of photogrammetry, which is known as stereophotogrammetry or stereo imaging, is applied. This form of photogrammetry involves the use of two or more images that were taken from different positions but have a certain amount of overlap (‘stereo pairs’). This enables the identification of common points on each image, after which a line of sight can be constructed from the sensor

location to these specific points. Triangulation based on the intersection of these lines of sight allows for determining the three-dimensional coordinates of the point, which can then be converted to a geodetic reference system to give the elevation data meaning.

Due to the vast amount of data processing that is required for stereo imaging and stereo image pairing, a large share of the currently available digital elevation datasets uses a form of automated stereo correlation techniques. Quincey et al. (2014) emphasize, however, that the quality of these elevation datasets largely depends on knowledge of the exact image and terrain geometries at the time of acquisition and automated stereo image pairing is therefore prone to error. Hence, knowledge about the automated processes and validation of the used DEMs in the form of an accuracy assessment are highly desirable (see, for example, Hirano et al., 2003; Fujisada et al., 2005 and Tachikawa et al., 2011).

One of the most popular sources of elevation data that makes use of photogrammetric processing and automated stereo correlation techniques is the imagery captured by the Advanced Spaceborne Thermal Emission and Reflection Radiometer (ASTER) sensor aboard the Terra satellite that was launched by the US National Aeronautics and Space Administration (NASA), in cooperation with Japan's Ministry of Economy, Trade and Industry (METI) in 1999 (see Yamaguchi et al. (1998) for a technical overview). One of the derived products from this satellite mission is the Global Digital Elevation Model (GDEM).

The ASTER sensor provides image data in a total of 14 spectral bands, 3 of which are in the visible/near-infrared wavelength region (Hirano et al., 2003). The stereo image data that is used for the creation of the GDEM only stems from this wavelength region and is recorded using a coupled nadir and backward-looking telescope system (see Figure 2). There is a difference of circa 60 seconds between the time the nadir telescope passes over a ground location and the backward-looking telescope records the same location on the ground track of the satellite. This set-up is ideal for generating DEMs by automated stereocorrelation techniques for various terrain conditions because images are acquired under uniform environmental and lighting conditions (Quincey et al., 2014).

The combination of its sensor systems (with an adjustable sensor gain setting for increased contrast over ice and snow surfaces), its stereo-imaging capability, and the

public availability of various output products has made ASTER a favored instrument for glacier remote-sensing studies, especially the GDEM product, which is widely used for the derivation of glacier parameters, such as elevation (Ramachandran et al., 2014).

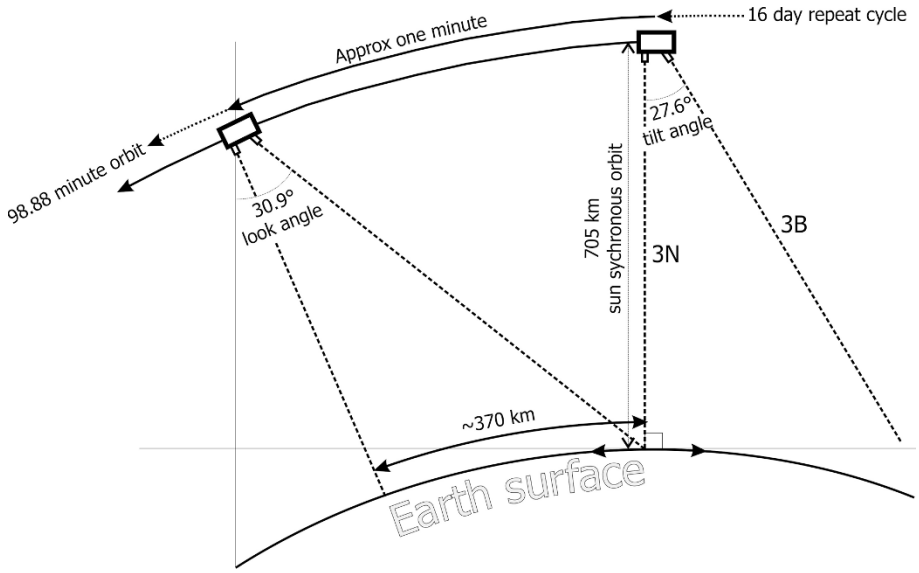

Figure 2. *Configuration of the stereo-imaging capability of the ASTER sensor, on board the Terra satellite. The ASTER sensor is equipped with two-directional sensors in the near-infrared: one at nadir (3N) and one backward looking (3B) (after Quincey et al., 2014).*

2.4 Light detection and ranging (LiDAR)

LiDAR is a surveying method that measures distance to a target by illuminating the target with pulsed laser light and measuring the reflected pulses (or backscatter) with a sensor. Differences in laser return times and wavelengths can then be used to make digital representations of the target (Shan & Toth, 2008). LiDAR applications can be divided into airborne, spaceborne and terrestrial types, all of which are increasingly used in the field of geosciences (Komar, 2017). Compared to traditional analogue or digital (passive) optical remote sensing, LIDAR offers many advantages, including nearly perfect registration of spatially distributed features and the ability to perform topographic measurements with very high precision and accuracy. This is also visible in LiDAR-based DEMs, which are of a relatively high quality and allow for improved geomorphometric characterization of the terrain and glacier surfaces (Quincey et al., 2014).

In glaciological applications, airborne LiDAR (sometimes simply referred to as Airborne Laser Scanning (ALS)) is the preferred method (e.g. Arnold et al., 2006b; Telling, et al, 2017). A LiDAR system operating from an airborne platform comprises a set of instruments: the laser device, an inertial navigational measurement unit (IMU), which continuously records the aircraft's orientation, a Global Navigation Satellite System (GNSS) unit (in most cases the Global Positioning System (GPS) is used), which records the three-dimensional position of the aircraft, and a computer interface that manages communication among devices and data storage. The system also requires a GNSS base station installed at a known location on the ground in order to differentially correct the airborne GNSS data (see Figure 3). In topographic mapping applications (e.g. DEMs), the wavelength of the pulses that are sent by the laser device is usually in the near-infrared part of the electromagnetic spectrum, typically between 1040 and 1065 nm (Shan & Toth, 2008).

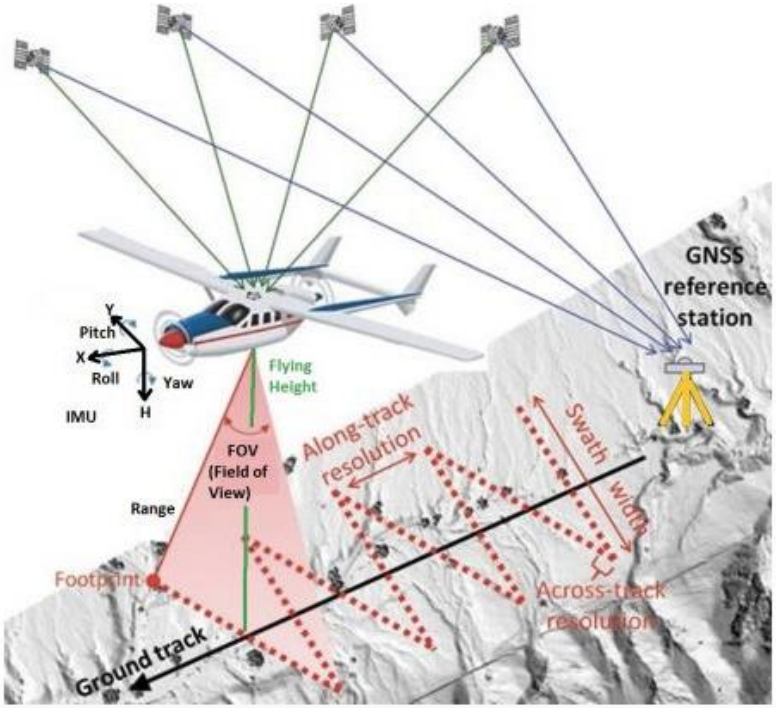

Figure 3. *ALS configuration.* The GPS base station and the on-board IMU enable automatic calculation of the X,Y,H coordinates of ground points from range and scan angle (Lemmens, 2017).

2.5 Digital elevation models (DEMs)

At its core, a DEM is a digital representation of the land surface elevation with respect to a common (vertical) reference datum such as the World Geodetic System or the European Terrestrial Reference System. A DEM solely represents the surface of the bare earth. Nevertheless, one will find that the term DEM is commonly used to refer to any digital representation of a topographic surface and seems to be accepted as a generic term covering digital topographic data in all its various forms as well as the method for interpreting the elevations between observations (Maune, 2007).

Depending on the source and/or preferred method of analysis, a DEM can be constructed either as a raster-based cell grid, which is a regular matrix with each cell (or pixel) representing elevation values, or as vector-based models such as a triangulated irregular network (TIN) or contour lines (Moore et al., 1991) (see Figure 4). The TIN model represents the surface as a set of irregularly distributed nodes and lines with x, y and z coordinates that are arranged in a network of non-overlapping triangles. Within each triangle, a plane (the face of the triangle) represents the surface and each vertex is a known (i.e. observed) elevation value. The contour structure is based on the concept that land surface can be divided into small, irregular shaped polygons based on contour lines and their orthogonals. TIN elevation models have its limitations when it comes to spatial analysis but continue to be popular in terrain modelling because of the frequent usage of LiDAR and the topological limitations that come with regular gridded raster-based DEMs (Ali & Mehrabian, 2009).

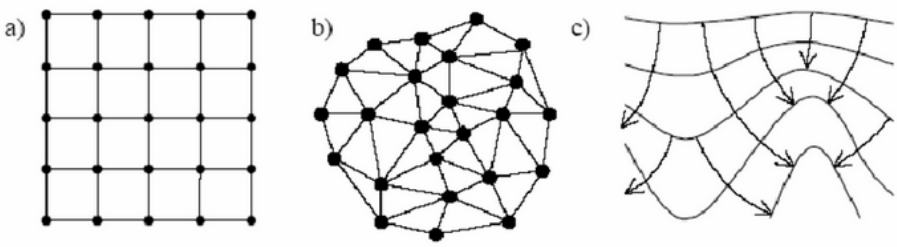

Figure 4. *Typical DEM data structures: a) raster-based cell grid; b) vector-based TIN or c) contours (after Masini et al., 2011).*

Another advantage of using a TIN over a raster-based DEM in mapping and analysis is that the points of a TIN are distributed variably based on an algorithm that determines which points are most necessary to create an accurate representation of the land surface. This means data input is flexible and fewer points need to be stored than in a raster-based DEM with regularly distributed points, which may reduce file size and save time during image processing. Moreover, raster-based DEMs have the disadvantage that they appear as a continuous elevation surface although in reality they are not, due to the limitations of the cell size of the grid. Abrupt elevation changes or a complex relief, for example, might therefore not always accurately appear in the derived DEM (for these and other scale or resolution effects, please refer to section 2.6.3). Nevertheless, choosing to represent digital topography in either vector or raster format really depends on the type of analysis a user wants to perform. Especially for the analysis of physical features, such as precipitation, vegetation type or general land cover classification, rasterized DEMs are often considered to be more suitable (Khorram et al., 2012).

2.5.1 The use of DEMs in glaciology

DEMs are widely used in glaciological applications nowadays. Some studies have used DEMs to extract indices of glacier topography, such as slope and aspect, which were then combined with satellite images to map glacier areas (e.g. Kääb et al., 2002; Paul et al., 2002). Also, a lot of research has been done on ways to assess glacier mass balance and volumetric change by using time series of digital elevation data. Etzelmüller (2000), for example, conducted research in which DEMs have been used as tools to derive hypsometry maps at different time steps and to quantify vertical surface changes on glaciers in remote areas, as indirect measurements of mass balance. Neelmeijer et al. (2017) also show how DEMs that are generated with the aid of remote sensing devices can be powerful data sources to infer glacier elevation changes in remote and mountainous areas.

Besides the more traditional approaches like surveying and monitoring, DEMs are also increasingly popular as input data for automated processes and computational modelling in the field of glaciology. James & Carrivick (2016) show that with high-resolution DEMs, which permit accurate calculation of surface slope, perfect plasticity-based models are becoming popular to model distributed ice thickness, volume and bed topography of glaciers. These models require only glacier outlines, centrelines and a

DEM. Because of the relative simplicity of the calculations combined with wide availability of input data, these models are often a better choice than models for viscous flow mechanics when considering large regions, according to the authors. Another example comes from research done by Le Bris & Paul (2013). They point out that glacier length (as a flow line) is a key parameter in global glacier inventories but difficult to determine in a consistent way and seldom available from digital databases. To overcome this hiatus, they present an algorithm that calculates a reasonable and reproducible scalar value and vector segment for glacier length based only on a DEM and glacier outlines as input.

2.6 Quality assessment of DEMs

Although a DEM is a model of the elevation surface, it is often not treated as a model but rather it is accepted as a true representation of the Earth's surface. However, elevation data in DEMs are without exception subject to error and uncertainty (Wechsler & Kroll, 2006). As mentioned before, main sources of error in DEMs include those derived from variations in the accuracy, density and distribution of the measured source data and possible (systematic) biases during data acquisition, those derived from data processing and interpolation, and those resulting from the characteristics of the land surface and, hence, the spatial resolution (Fisher & Tate, 2006).

In the literature on quality assessments of DEMs, the concepts 'error', 'accuracy', and 'uncertainty' are often poorly defined or applied in an imprecise way. The terms are sometimes even used interchangeably. In this thesis, error is defined as the (known) difference between an observed value and its corresponding true value (after e.g. Wechsler & Kroll, 2006). Accuracy is defined as the level of agreement between an observed value and its true counterpart (after e.g. Mukherjee et al., 2013). Uncertainty is the unknown (range of) difference between an observed value and its true value. In other words: there is a lack of knowledge and it could therefore be argued that error constitutes uncertainty. It should be mentioned, however, that some studies in the field of quality assessment of DEMs point out that there is often a discrepancy when it comes to the proper use of the term 'error'. This results from the fact that accurate knowledge about error – and especially its actual measurement - would require true elevation data, something which is rarely determinable (Goodchild et al., 1994; Hunter et al., 1995). Some authors thus argue that, instead of error, uncertainty should be used to describe the

quality of a DEM (see e.g. Weng, 2002). Nevertheless, for the quantification and evaluation methods in this thesis the term ‘error’ is preferred over the term ‘uncertainty’ because, essentially, ‘true’ elevation data is by definition an approximation due to the nature of its construct. Reference data such as GPS-based or ALS-based elevation measurements, which serve as such an approximation in the comparison with the observed data, could therefore equally serve as ‘true’ elevation data. For the quantification and evaluation methods, it is the (known) difference between both data sources that matters.

2.6.1 Spatial accuracy

Evaluation of the spatial accuracy of elevation data is a key research issue in the area of quality assessment of DEMs (Shi et al, 2004). The spatial accuracy of DEMs is primarily assessed by looking at the horizontal and vertical accuracy of the elevation data. Horizontal accuracy relates to the true position of features in the landscape and can be expressed as the difference between the measured horizontal position of a feature and its “true” position (with reference to the same geodetic datum). Most studies on the accuracy of DEMs are focussing on vertical accuracy, which can be expressed as the difference between the measured elevation of a feature and its “true” elevation (again, with reference to the same geodetic, i.e. vertical, datum). Vertical accuracy is determined by many factors, including the functioning of the remote sensing device. For example, Braun & Fotopoulos (2007) show that certain radar signal measurements inherent to the specifications of the sensors that were used for the Shuttle Radar Topography Mission result in a typical sensing of surface features, depending on terrain cover (e.g. ice, snow, sand, vegetation, etc.). In snow, for example, the penetration depth of the radar signal depends on wetness, temperature and porosity. The fact that debris cover changes this penetration depth complicates the measurement of vertical accuracy even further (Vijay & Braun, 2016).

2.6.2 Interpolation methods

Restricted by the spatial resolution of the remote sensing device, elevation values per grid cell in a raster-based DEM or the values of converted elevation data point clouds are typically determined by interpolation and approximation methods, such as linear prediction, spline interpolation, TIN interpolation, kriging or inverse distance weighting (IDW) (Bater & Coops, 2009). The latter two methods particularly rely on Tobler’s First

Law of Geography: "Everything is related to everything else, but near things are more related than distant things." (Tobler, 1970, p.236). This first law is the foundation of the concepts of spatial dependence and spatial autocorrelation. IDW is the simpler of the two methods. It involves using known z-values and weights determined as a function of distances between the unknown and known points. In general, this means that the greater the distance between two points, the smaller the mutual influence, depending on an exponent that is predefined. IDW differs from kriging in that no statistical models are used.

Kriging is most appropriate when there are spatially correlated distances or directional biases in the data. Like IDW, kriging forms weights from surrounding measured values to predict unmeasured points. The measured values closest to the unmeasured points have the most influence on these points. Kriging, however, uses a statistical method that makes use of variograms to calculate the spatial autocorrelation in order to determine the weights that should be applied at various distances (Liu et al., 2007).

Both kriging and IDW are very functional and widely used interpolation methods for elevation data. However, if the measured land surface has a lot of abrupt changes in elevation and no continuous elevation data is required, TIN interpolation can be the better choice. As described in section 2.5, a TIN is built up from a network of triangles that connect all elevation data points. In the TIN interpolation method, the values of the grid cells are calculated using the slope and shape of the triangles. The maximum length of the triangle sides and an exponent are predefined. TIN interpolation is therefore able to incorporate discontinuities and is efficient to represent rough terrains because the density of the triangle can be varied easily (Bater & Coops, 2009).

The selection of an appropriate interpolation method for the creation of a DEM is often an important decision, not least because accuracy of the elevation data within the model directly affects the estimates of topographic parameters. Racoviteanu et al. (2007) highlight the importance of this issue in glaciology by describing an example in which time series analysis of glacial change is based on the combination of satellite-derived DEMs and DEMs based on digitized elevation contours from old topographic maps. The authors point out that there is no established interpolation method especially suitable for creating continuous elevation data from old topographic maps. And, although the

accuracy of various techniques to construct DEMs from digitized contour data has been addressed in the literature, the glaciological community has yet to agree on a suitable interpolation method. Nevertheless, several attempts were made. For instance, Etzelmüller & Björnsson (2000) used IDW to create a continuous surface from radar profile lines on a glacier, Mennis & Fountain (2001) used spline interpolation for the representation of glacier and sub-glacier topography and Gratton et al. (1990) applied a TIN interpolation, derived from digitized contours, to represent rugged glacier topography at the Columbia Icefield in Canada.

2.6.3 Scale effects and spatial resolution

The effect of scale on geospatial data and data processing is an unavoidable issue in geosciences and, according to Quattrochi & Goodchild (1997), has been well recognized as one of the more fundamental aspects of any research within the field. This also holds true for topographic analysis and modelling. As such, derivatives of a DEM, e.g. topographic parameters, are also essentially controlled by the scale factor: when the spatial resolution of a DEM is coarsened, the topographic parameters may subsequently be varied in different ways (Chen & Zhou, 2013).

A wide variety of research is done that investigates the effect of spatial scale and resolution on topographic analysis and modelling. Hasan et al. (2012), for instance, focus on variations in the estimation of slope, drainage area and topographic wetness index as a result of different DEM resolutions. They find that these estimations differ significantly with the resolution of the DEM. Research done by Chang & Tsai (1991) showed that both the accuracy of slope and aspect decline with coarser DEM resolution. A study by Gao (1997) also evaluated how spatial resolution affects the accuracy of surface representation for three areas with different types of topography. He found that DEM resolution has an impact on mean slope and even more so on the standard deviation of slope. Chow & Hodgson (2009) describe how some researchers even initiated attempts to identify the optimal scale, which may best capture the surface complexity with the least error.

Most of the scale effects that occur when using DEMs for topographic analysis are directly linked to spatial resolution. For the last few decades, spatial resolution has been the main limitation in terms of accuracy of remote sensing in glaciological applications (Kääb et al., 2005). Spatial resolution of a DEM generally refers to the dimension of the

cell (pixel) size representing the area covered on the surface. The higher the spatial resolution of a raster, the smaller the cell size and, thus, the greater the detail. This means that the more homogeneous an area is for specific variables such as topographic features or land use, the larger the cell size of the DEM can be without affecting accuracy.

Note that a distinction can be made between spatial resolution and cell or pixel size. Although the terms are often used interchangeable, strictly speaking the spatial resolution refers to the smallest identifiable feature on a satellite image and is not necessarily the size of the pixel. Landforms and features must therefore often exceed the pixel size in order to be visible on the images. Pixels that contain more than one surface type or elevation value can wrongfully be assigned in the elevation model, which, over the whole image, can create a considerable error and segmentation (see Figure 5). As a result, some resolutions may be adequate for medium- or large-sized glaciers but might struggle capturing smaller ice masses such as alpine glaciers or other glacier parameters such as surface velocities or mass balance (Gao and Liu, 2001).

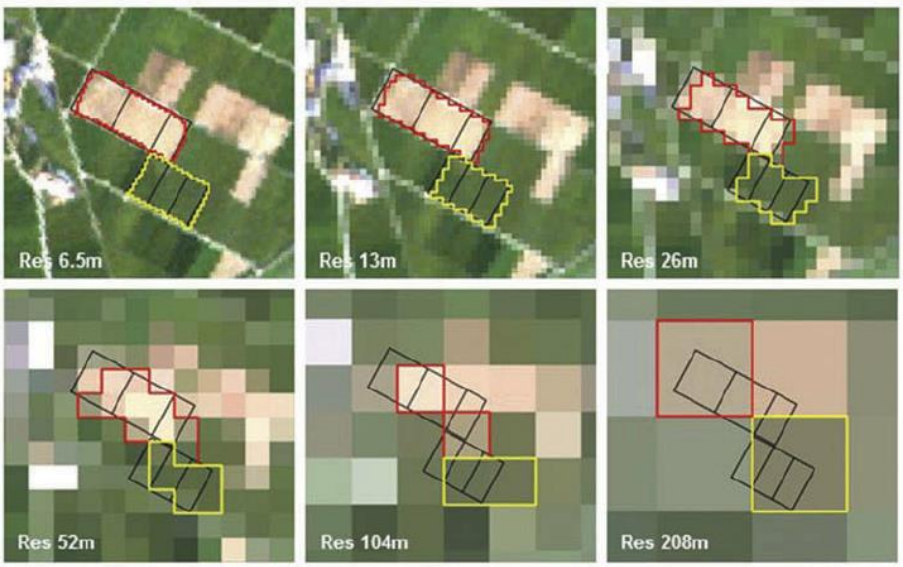

Figure 5. *Example of segmentation results as spatial resolution is altered. The highest resolution (6.5 m) yields the most detailed image (after Kim, 2014).*

3. DATA AND METHODS

3.1 Study area: Hintereisferner

Having been subject to ongoing observations and measurements for many decades now, the Hintereisferner glacier has an impressive track record as object of scientific research and is perhaps among the glaciers with the longest period of continuous study in the world (i.e. research based on validated and consistent methods of observation). First documentation of change observations in the area of Hintereisferner even dates back to the early 19th century (Strasser et al., 2018). The glacier is still extensively studied and has been the object of a variety of remote sensing data products.

Hintereisferner (46°48’0”N, 10°46’12”O) is situated in the mountain range Ötztal Alps and is one of the largest glaciers in Tyrol, Austria (figure 6a and 6b). It covers an area of about 7 km^2.

Figure 6a. *Overview of the European Alps with the approximate location of the Hintereisferner glacier (source: Google Earth).*

Figure 6b. *Part of the Austrian Alps where the Hintereisferner glacier is located. Outlines for the glacier are based on GLIMS glacier inventory (source: Google Earth / Fischer (2012)).*

The outline of the study area is based on shapefiles that are provided by contributors to the GLIMS glacier inventory project (Fischer, 2012).

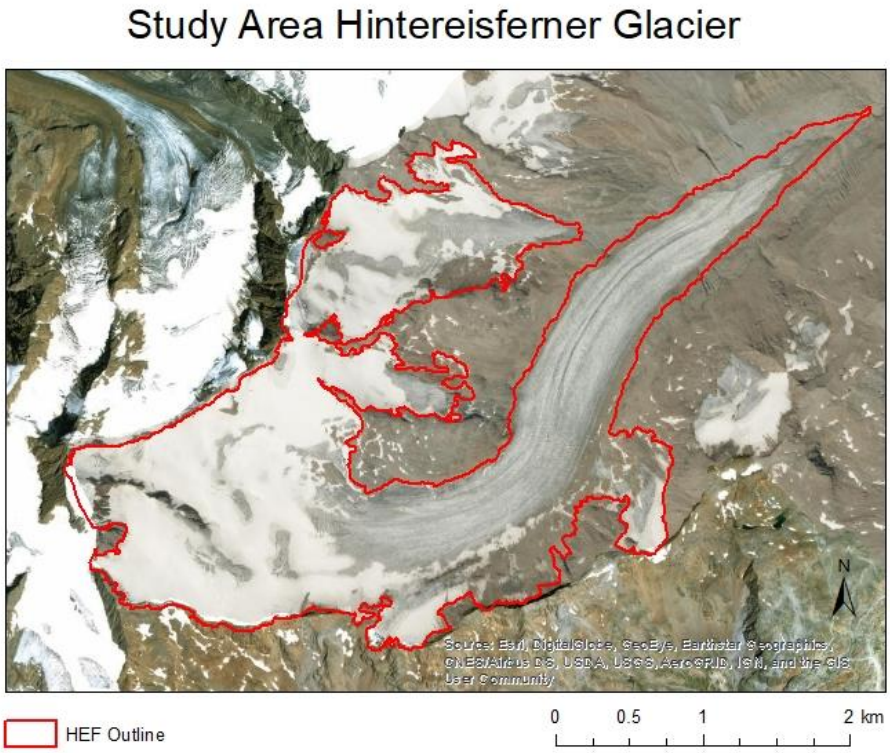

Figure 6c. *Spatial extent of the study area. The outline of the glacier equals the outer boundary of the DEM data on which the analyses will be performed (source: Google Earth / Fischer (2012)).*

3.2 Remote sensing data

The feasibility of this study largely depends on the availability of high-quality reference elevation data for glacial areas on the one hand, and that of freely available DEMs with matching spatial and temporal coverage on the other. Many publicly available DEM data sources exist but there are limitations when it comes to spatial and temporal resolution and coverage. The SRTM, for example, generated a very complete and, at least for that time, relatively high-resolution topographic dataset of Earth in the early 2000s. But the spatial scale ranged only from 56°S to 60°N, which means that a lot of places where glaciers are abundant (e.g. Alaska at ca. 61°N and up) are not included in the data.

To be able to spatially and temporally match potentially suitable DEM data sources with high-resolution reference data, the data acquisition for this study is based on the least available data as a starting point and is then complemented with the more widely available data. This results in the following datasets that will serve as input in the comparison to find error and to compile (derived) topographic parameters:

(i) A set of imagery tiles from the Advanced Spaceborne Thermal Emission and Reflection Radiometer Global Digital Elevation Model (ASTER GDEM), version 2, which is a product of METI and NASA. The data is ordered for free from NASA's Land Processes Distributed Active Archive Center.

(ii) LiDAR-derived (i.e. ALS-based) raster DEM data for the Hintereisferner glacier, which are produced and made available by the University of Innsbruck (Sailer et al., 2017).

The rasterized LiDAR data - which serves as reference data - is projected in the Universal Transverse Mercator (UTM) system, zone 32N, and uses the European Terrestrial Reference System 1989 (ETRS89) as (geodetic) coordinate reference system. The data from ASTER GDEM will be converted to match these projected and geographic reference systems.

3.2.1 ASTER GDEM

The Terra satellite carrying the ASTER sensor is part of a joint mission between Japan and the USA and has a coverage range of 83°S to 83°N, which means it includes a large part of the Polar Regions and Alaska's glaciers. Due to the wide range of imaging bands, the spatial resolution ranges from 15 to 90 m but final output for the GDEM product has been delivered in 1" (i.e. 30 m). The data was released to the public in 2009 and received a considerable update in 2011 with a lot of substantial improvements in quality of the DEM. Vertical accuracy fluctuates but is in the order of approximately 5-15 m (with 8.3 m as an average of the mean of elevation error), based on the validation report for GDEM Version 2 by Tachikawa et al. (2011). This broad range in accuracy covers factors like variation in land cover, penetration depth, atmospheric conditions, etc. Because the accuracy is non-uniform within each subset of data, a lot of research has been conducted to estimate vertical accuracy of the ASTER GDEM data for specific circumstances. Mukherjee et al. (2013), for instance, find an overall vertical accuracy of ca. +/- 12 m for parts of the Himalaya in India. Table 1 shows the specifications of the ASTER GDEM data that is used in this study.

Table 1. *Specifications of the ASTER GDEM dataset used in this study.*

Entity ID	Sensor/band	Resolution	Datum	Acquisition
N46E010	ASTER, VNIR band B3N, B3B (near infrared)	1 arc-second	WGS84 (horizontal) EGM96 (vertical)	17 Oct 2011

3.2.2 LiDAR

The specific LiDAR dataset for the Hintereisferner that is used in this study was acquired in 2011 as part of the Austrian Space Applications Program (Project Nr.: 815527), funded by the Austrian Research Promotion Agency (FFG). The elevation data are comprised of a series of point measurements recorded from an aircraft and saved in a file format (e.g. LAS) that can easily be converted into 3D point cloud data, which serve as the input data for the raster DEM. The vertical accuracy, expressed as standard deviation, has been determined to be around 0.04 m for this dataset. The raw LiDAR point cloud data were converted to 1x1 m raster DEMs by Sailer et al. (2017). This was done by calculating z-

values (elevation) from the mean z-value by excluding 5 % of the lowest and highest observations of the ALS points which fall inside the respective grid cells. For this dataset, the shoot density (mean points density) of the ALS device has a value of 2.9 points per m^2. Ideally, the number of grid cells in a raster DEM is at least about the same as the number of data points representing the terrain area, given there is a more or less homogeneous distribution of data points (see e.g. McCullagh, 1988). A mean point density of 2.9 per m^2 should therefore, in principle, be sufficient for a raster DEM with a 1x1 m cell size, although this also depends on altitude of the platform and footprint size. Moreover, LiDAR data with a high point density typically do not need interpolation and therefore preserve small-scale features and their impact on the subtle local variations in slope and aspect over the glacier surface, provided that the spatial resolution is high enough to capture these features (Arnold et al., 2006b). Table 2 shows the specifications of the LiDAR data.

Table 2. *Specifications of the LiDAR dataset used in this study.*

Entity ID	Sensor/band	Resolution	Datum	Acquisition
HEF21_2011-10-04_r1	Teledyne Optech ALTM 3100	1 m	ETRS89	4 Oct 2011

3.3 Data preparation

Preparation and processing of the data is done with the aid of geospatial processing software (ArcGIS), a statistical software package (IBM SPSS), and spreadsheet software (Microsoft Excel). Data preparation mainly concerns the standardization of the two elevation data sources in terms of spatial projection, reference system, file format, and extent (see Figure 6c). Also, a vector grid of sample points is created to be able to spatially match the coarse ASTER GDEM elevation data to the reference data, which has a much finer resolution. Processing of the data includes the compilation of a derived topographic parameter, i.e. slope, and resampling and interpolation of the raster files. The resulting characteristics of the datasets after preparation are detailed below (Table 3).

Table 3. *Data specifications of the different DEMs after data preparation.*

Source	Projection	Datum/Ellipsoid	Initial cell size	Cell size	Data type**
ASTER GDEM	UTM 32N	ETRS89/GRS80	1 arc-second	26.16861243 m*	Integer
LiDAR	UTM 32N	ETRS89/GRS80	1 m	1 m	Integer (converted)

** The precise cell size value has been maintained to avoid rescaling issues.*

*** Due to its resolution and margin of error, the elevation values in the ASTER GDEM dataset are only available as integer. For the purpose of this study, the floating-point LiDAR data is converted to integer to match the data type of the ASTER GDEM dataset. This results in a maximum loss of detail of +/- 0.5 m per cell.*

3.4 Compilation of derived topographic parameters

Derived topographic parameters (also known as topographic indices or geomorphic metrics) are compiled to complement the information provided in a DEM through mathematical transformations of elevation data. They are used in many scientific applications such as hydrology, geomorphology, and glaciology. In ice-sheet modelling, for example, elevation data help to determine locations at which positive mass balance will allow accumulation. This is done by combining the derived topographic parameter surface slope and ice sheet thickness in order to derive the driving stress of the ice sheet (Hebeler & Purves, 2009).

A relatively small number of topographic parameters together form the core of the description of a DEM. These often include elevation, slope, and aspect. Two of these core parameters will be used within the context of this study. The most important one, elevation, is the main element in the error quantification, whereas the derived topographic parameter, slope, serves as a proxy for spatial resolution effects.

3.4.1 Slope

The slope is calculated as the maximum rate of change in elevation value in the horizontal and vertical directions between each raster cell and its neighbouring cells. Basically, this

means that the maximum change in elevation over the distance between the cell and its eight neighbours equals the steepest downhill descent from the cell. The calculation is performed on a projected flat plane using a 2D Cartesian coordinate system (the so-called planar method). At every cell in a raster-based DEM the slope (S) can be defined as a function of gradients in the X and Y directions:

$$S = \arctan\left(\sqrt{\left(\frac{dz}{dx}\right)^2 + \left(\frac{dz}{dy}\right)^2}\right) \times \frac{180}{\pi} \tag{1}$$

where $\frac{dz}{dx}$ and $\frac{dz}{dy}$ are the perpendicular gradients (rate of change) in horizontal and vertical direction and S is expressed in units of degrees. The key in slope estimation is the computation of these perpendicular gradients. Different algorithms use different techniques to estimate them, resulting in a diversity of estimated slope values. According to Tang et al. (2013), from a raster-based DEM the common approach when estimating the gradients is to apply a moving 3 by 3 window to derive the finite differential or local polynomial surface fit for the estimations (see Figure 7). The cells in the outermost rows and columns of the output raster will not get any data values assigned. This is because the cells along the boundary of the input dataset do not have enough valid neighbours to perform calculations. To bypass this problem, the spatial extent of the area on which the slope calculations are performed is slightly larger than the actual extent of the study area.

A	B	C
D	E	F
G	H	I

Figure 7. *The values of the center cell and its eight neighbors determine the horizontal and vertical gradients.*

In Figure 7, the neighbouring cells are identified as letters from A to I, with E representing the cell for which the slope is being calculated. The rate of change in the horizontal direction for cell E is calculated with the following equation:

$$\frac{dz}{dx} = ((C + 2F + I) * \frac{4}{\alpha} - (A + 2D + G) * \frac{4}{\beta} \ / \ (8 * cellsize(x)) \qquad (2)$$

where α and β are the horizontal weighted counts of valid cells. For instance, if C, F, and I all have valid values then $\alpha = (1 + (2 * 1) + 1) = 4$. But if C has no elevation value then $\alpha = (0 + (2 * 1) + 1) = 3$.

The rate of change in the vertical direction for cell E is calculated in a similar way:

$$\frac{dz}{dy} = ((G + 2H + I) * \frac{4}{\gamma} - (A + 2B + C) * \frac{4}{\delta} \ / \ \left(8 * cellsize(y)\right) \qquad (3)$$

3.5 Error quantification and evaluation

There are many ways to estimate the (vertical) accuracy of a DEM in terms of error, or the level of agreement between elevation values from different datasets. Most of them are based on regular statistical model validation techniques. Cross-validation, for example is often used in settings where the goal is prediction of unknown values and one wants to estimate how accurately a predictive model will perform in practice. The model is usually given input data with a known high quality and accuracy (e.g. LiDAR or differential GPS elevation data) on which training is run with a training dataset, and a dataset of unknown data against which the model is tested (i.e. the validation dataset).

This study focuses on quantifying and evaluating error in the elevation values, which is represented by the vertical coordinate (z-value) in the elevation model - the only unconstrained coordinate value in the raw data. The z-value is of particular interest in glaciological applications, e.g. because surface elevation changes over time can be an indicator for mass balance changes. In this study, two commonly used methods or measures are applied as a starting point to quantify and evaluate the error that is present in the ASTER GDEM elevation data for the Hintereisferner. These methods are selected based on the relevant scientific literature (e.g. Weng, 2002; Carlisle, 2005; Wechsler & Kroll, 2006; Fisher & Tate, 2006; Erdogan, 2010; Gonga-Saholiariliva et al., 2011; Mukherjee et al., 2013) and include:

(i) Root mean square error (RMSE)

(ii) Correlation analysis

In addition to these conventional methods of error quantification in DEMs, two methods are included that give insight into the spatial distribution of the error:

(iii) Error surfaces

(iv) Measures of global and local spatial autocorrelation and clustering

Finally, two methods of error quantification and evaluation are applied that cover interpolation effects and spatial resolution effects. These two effects have been identified earlier in this study as major sources of error in DEMs.

(i) In geosciences, one of the most commonly used measures of error is the RMSE. Its values can be calculated by comparing the differences between the elevation values and

the ones from the reference data. This will yield a very easily understood "average error". The RMSE is expressed as:

$$RMSE = \sqrt{\frac{\sum_{i=1}^{n}(y_i - yt_i)^2}{n}} \tag{4}$$

where y_i refers to the ith estimated or modelled elevation ("predicted"), yt_i refers to the ith known or measured elevation ("observed"), and n is the number of sample points.

RMSE measures how much error there is between two data sets. In other words, it compares a predicted value and an observed or known value. In this study, the predicted value is ASTER GDEM elevation data and the observed value is LiDAR elevation data. RMSE quantifies the difference between sets of values. The smaller an RMSE value, the closer predicted and observed values are, but the absolute RMSE value has only meaning in relation to the range of the predicted values (in this case the low-resolution elevation data). Wechsler & Kroll (2006) point out that the RMSE itself therefore does not provide an accurate assessment of how well the DEM represents true elevation. Note that the correlation analyses and RMSE values contain no information about the spatial distribution of error, which is often spatially correlated with topographic parameters. Rather, estimates of uncertainty based on RMSE assume a uniform error value. Several studies have shown that this is often not the case (see e.g. Weng (2002); Erdogan (2010)).

(ii) Correlation analysis is a method of statistical evaluation used to examine the strength of a relationship between two, numerically measured, continuous variables (e.g. elevation or slope). This particular type of analysis can be helpful to determine if there are possible connections between these variables. In this case, the comparison is applied on elevation as the topographic parameter in the low-resolution ASTER GDEM data and the high-resolution LiDAR reference data. To keep the amount of data manageable, sampling is applied. A grid of sample points is created with a fixed interval and equal spatial distribution to avoid biased sampling. The Pearson correlation coefficient (Pearson's r) is calculated as a measure of the linear correlation and used to quantify the strength of the correlation and its direction. Line fitting with an ordinary least squares approximation is

added to the scatter plot for visualization purposes. Pearsons's r, when applied to a sample, is defined as:

$$r_{xy} = \frac{\sum_{i=1}^{n}(x_i - \bar{x})(y_i - \bar{y})}{\sqrt{\sum_{i=1}^{n}(x_i - \bar{x})^2}\sqrt{\sum_{i=1}^{n}(y_i - \bar{y})^2}} \tag{5}$$

where n is the sample size, x_i, y_i are the individual sample points from the sample grid with 50m interval, and $\bar{x}$, $\bar{y}$ are the sample mean.

(iii) One of the most effective ways to observe and analyse the spatial distribution of error in DEMs is to create a visualization of the error values in the form of an error surface (Fisher & Tate, 2006). DEMs error surfaces are constructed by subtracting the high-resolution reference raster DEMs from the ones with a coarse resolution on a cell-by-cell basis. The coarser ASTER GDEM raster is resampled to the cell size of the reference DEM to enable a direct subtraction. Nearest neighbour resampling is applied because it maintains cell values if the centre of the raster cell in the output coincides with the input cells. The maximum spatial error will therefore be reduced to half the cell size. In general, this would be problematic because it compromises the elevation values in the DEM. In this case, however, the measures - which are: absolute error values per raster cell and its spatial distribution - are not altered.

(iv) The analysis of the spatial distribution of error, especially visualization and quantification of spatial autocorrelation, helps measuring the degree of clustering and locates weaknesses and inaccuracies in the spatial structure of the DEM. It highlights the spatial heterogeneity of error and helps determine potential locations that may require data correction (Gonga-Saholiariliva, 2011). To quantify the spatial distribution of error, four measures of spatial autocorrelation are used. Two of them are global: Global Moran's I and Getis-Ord General G. The other two are local: Local Moran's I, and Getis-Ord Gi*. Although all four measures examine the extent of error clustering, they differ in the way they represent this.

Calculations of all measures of spatial autocorrelation and clustering are based on a vectorized error surface containing a total of 346,762 polygons. The initial error surface contains 7,466,365 cells (data points) in total. Spatial relationships and threshold

distances for all measures are defined and set to values that ensure every input feature has at least one corresponding neighbor feature on which their spatial relationship is based, and, at the same time, minimize computations because of the vast amount of data points.

Global Moran's I is an indicator for error clustering for the entire DEM. It is calculated as follows:

$$I = \frac{n}{S_0} \frac{\sum_{i=1}^{n} \sum_{j=1}^{n} w_{i,j} z_i z_j}{\sum_{i=1}^{n} z_i^2} \tag{6}$$

where z_i is the deviation of an attribute (i.e. error value) for feature (i.e. polygon) i from its mean, $w_{i,j}$ is the spatial weight between feature i and j, n is the total number of features, and S_0 is a term for the aggregate of all the spatial weights.

Moran's I values range from -1 to +1, where -1 indicates perfect dispersion (i.e. clustering of dissimilar values), 0 indicates a random spatial pattern, and +1 indicates clustering of similar values (strongly positive spatial autocorrelation). Moran's I indicates clustering but is not able to distinguish between clusters of high or low error respectively. Since the main interest in error evaluation for DEMs generally would be the presence of high error clusters, an additional measure of spatial autocorrelation is needed. The Getis-Ord General G measure can be used to check for concentrations of high or low error values, so-called 'hotspot analysis'. A high index value for the General G measure indicates clustering of high error values, whereas a low index value indicates clustering of low error values. It is expressed as:

$$G = \frac{\sum_{i=1}^{n} \sum_{j=1}^{n} w_{i,j} x_i x_j}{\sum_{i=1}^{n} \sum_{j=1}^{n} x_i x_j}, \forall j \neq i \tag{7}$$

where x_i and x_j are attribute values (i.e. error values) for features (i.e. polygons) i and j, and $w_{i,j}$ is the spatial weight between feature i and j. n is the total number of features, and $\forall j \neq i$ indicates that i and j cannot be the same feature.

Both Global Moran's I and the Getis-Ord General G yield only one single statistic that summarizes the whole DEM. They both fail to determine clustering at a local level. For this, Local Moran's I and Getis-Ord Gi* can be used. Local Moran's I and Getis-Ord Gi* are derived from the Local indicators of spatial association (LISA), a concept that Anselin (1995) came up with. Anselin based these indicators on the global Moran's I index to be able to identify local outliers or local clusters. In line with the global measures of spatial autocorrelation, the local ones can also be distinguished according to their type of output. The Local Moran's I is a measure to analyse clusters and outliers, whereas Getis-Ord Gi* is a measure for hotspot analysis. Local Moran's I is calculated with the following equation:

$$I_i = \frac{x_i - \bar{X}}{S_i^2} \sum_{j=1, j \neq i}^{n} w_{i,j} \left(x_j - \bar{X} \right) \tag{8}$$

where x_i and x_j are attribute values (i.e. error values) for features (i.e. polygons) i and j, $\bar{X}$ is the mean of these attribute values, $w_{i,j}$ is the spatial weight between feature i and j, and:

$$S_i^2 = \frac{\sum_{j=1, j \neq i}^{n} \left(x_j - \bar{X} \right)^2}{n - 1} \tag{9}$$

with n being the total number of features (i.e. the polygons).

Getis-Ord Gi* is calculated as follows:

$$G_i^* = \frac{\sum_{j=1}^{n} w_{i,j} x_j - \bar{X} \sum_{j=1}^{n} w_{i,j}}{S \sqrt{\frac{\left[n \sum_{j=1}^{n} w_{i,j}^2 - \left(\sum_{j=1}^{n} w_{i,j} \right)^2 \right]}{n - 1}}} \tag{10}$$

where x_j is the attribute value for feature j (i.e. error value), $\bar{X}$ is the mean of these attribute values, $w_{i,j}$ is the spatial weight between feature i and j, n is the total number of features.

The term S in the denominator is calculated as follows:

$$S = \sqrt{\frac{\sum_{j=1}^{n} x_j^2}{n} - (\bar{X})^2} \tag{11}$$

Although both Local Moran's I and Getis-Ord Gi* are used to analyze spatial patterns on a local level, the calculations each have different accents which leads to different results. For example, when Getis-Ord Gi* is calculated, each input feature value -in this case the error values of the polygons- is checked and the algorithm determines if each feature's neighborhood is significantly different from the study area. If so, the feature is categorized as part of a hot spot if the feature value is significantly higher or as part of a cold spot if the feature value is significantly lower. Local Moran's I algorithm, on the other hand, removes the feature from its neighborhood as a first step and then investigates if the neighborhood is significantly different from the study area. As a second step, the algorithm determines if each feature is significantly different from its neighborhood. This approach allows to find outliers within hot or cold spots, something the Getis-Ord Gi* algorithm is unable to do. Local Moran's I can therefore be useful when trying to find anomalies (for instance, polygons with significantly high error values in a neighborhood of polygons with significantly low error values).

3.5.1 Quantifying and evaluating interpolation effects

Major sources of error in DEMs are mentioned several times throughout this thesis. Interpolation of the elevation data, as part of the data processing, is considered one of these sources. The errors that arise because of interpolation effects often contribute significantly to the total error in DEMs. Because the commonly used, publicly available, DEMs with (near) global coverage, such as SRTM or ASTER GDEM, are usually provided with a maximum resolution of around 30 m, it is quite common for researchers to resample or interpolate the data (see section 2.6.2 for a description of interpolation methods). Theoretically, this enables data analysis at a more detailed level, provided the interpolation method yields accurate values.

As described earlier in the chapter on theoretical background, one of the more suitable interpolation methods for elevation data is kriging. This method is preferred in the case

of spatially (auto)correlated data, which is, as will become clear in the results on spatial distribution error later in this thesis, often an important characteristic of elevation data (see also Wechsler & Kroll (2006), who discuss the nature of elevation data in more detail).

Before kriging as interpolation method can be applied, the original raster elevation data from the ASTER GDEM dataset is vectorized to point features, one point for each raster cell. The elevation data values for the point features are based on the initial cell values. Kriging parameters are set to create an interpolated raster with an output cell size equal to the LiDAR-based reference DEM, i.e. 1 m, and a variable search radius that includes a default of 12 nearest input sample points to be used to perform interpolation. Because of possible edge effects around the glacier outline, the vectorisation of the DEM raster is based on a much wider spatial extent. After interpolation is applied, the output raster is clipped to match the outlines of the study area again.

In order to quantify and evaluate the effects on elevation values that are caused by the interpolation, a correlation analysis is applied in the same manner as is done for the initial error quantification in section 4.4, sub ii. This means the interpolated DEM is sampled with the same sample point grid, Pearson's r is calculated as a measure of the linear correlation, and a scatter plot is created for visualisation purposes and outlier detection. In addition, the RMSE value for the interpolated DEM is calculated. The reference data that is used for comparison is, again, the high-resolution LiDAR-based DEM.

3.5.2 Quantifying and evaluating spatial resolution effects

Besides errors due to interpolation effects, errors resulting from the characteristics of the land surface and, hence, the spatial resolution, are also high on the list of substantial sources of error in DEMs (Fisher & Tate, 2006). For example, if the maximum spatial resolution of a remote sensing device is 30 m and significant elevation changes occur within the spatial extent of only a few meters, then these changes are either not detected at all, or they are generalized to fit the resolution (see section 2.6.3 about scale effects and spatial resolution). In the case of glacier surfaces, one could think of crevasses, small ridges, medial moraines, or even small nunataks.

Spatial resolution effects can be highlighted by looking at certain derived topographic parameters, such as slope, because these parameters are particularly sensitive to abrupt changes in elevation because of the way they are calculated (the moving 3*3-window to calculate slope has been explained in section 3.3.1). Essentially, the derived topographic parameter slope serves as a proxy for relatively large elevation changes on a small spatial scale. This means that if one can find a strong correlation between slope values and error values, then this would be an indicator for the influence of spatial resolution effects on the error of the DEM. This is especially true if the correlation is still present and of high strength for areas with large variation in error values.

The idea of using certain topographic parameters or measures of morphology as a proxy to determine spatial resolution effects is not uncommon (see, for example, Mukherjee et al. (2013)). It should be mentioned, however, that using slope as a proxy to investigate spatial resolution effects should be treated with caution because it is evident that this approach does not exclude other sources of error such as interpolation effects. Indeed, errors or biases in the data acquisition could also very well propagate in this method.

In order to quantify and evaluate potential spatial resolution effects, slope values are calculated for the LiDAR-based reference DEM (see section 4.3.1). These slope values are then compared to the error values that result from the calculations that were made to create error surfaces (section 4.4, sub iii). A correlation analysis is applied to determine the strength and direction of the relationship. This analysis is based on a regular sample grid like the one that is used to extract values for the quantification of interpolation effects. Except in this case, the sample grid is denser with intervals of 25 m (instead of 50 m). The choice for a denser grid is based on the spatial extent of the parts in the study area that have a very high slope value and should ensure a proper sampling of these locations.

4. RESULTS AND DISCUSSION

4.1 Overview of the processed elevation data and descriptive statistics

Figures 8 and 9 show the ASTER GDEM-based elevation model for the Hintereisferner, which has a resolution of 1 arc second (ca. 26 m), and the LiDAR-based reference model with a 1 m resolution. Because of the relatively small spatial extent of the study area, the cell size for each individual pixel of the ASTER GDEM-based DEM is coarse enough to be visible on the map, whereas the reference DEM seems to be of a more continuous nature because of its much higher resolution.

Both maps show clearly distinct elevation levels throughout the study area. Most of the high elevation values can be found at the western parts of the study area or at the southern edges, while the lower elevation values are predominantly situated at the northeastern corner.

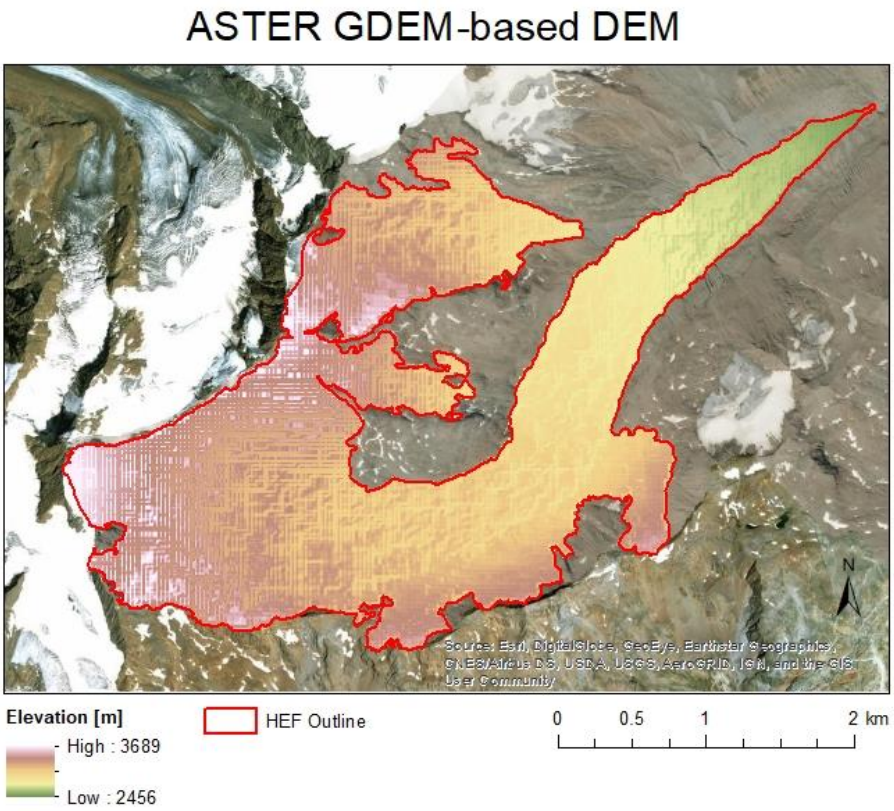

Figure 8. *Overview of the ASTER GDEM elevation data for the Hintereisferner.*

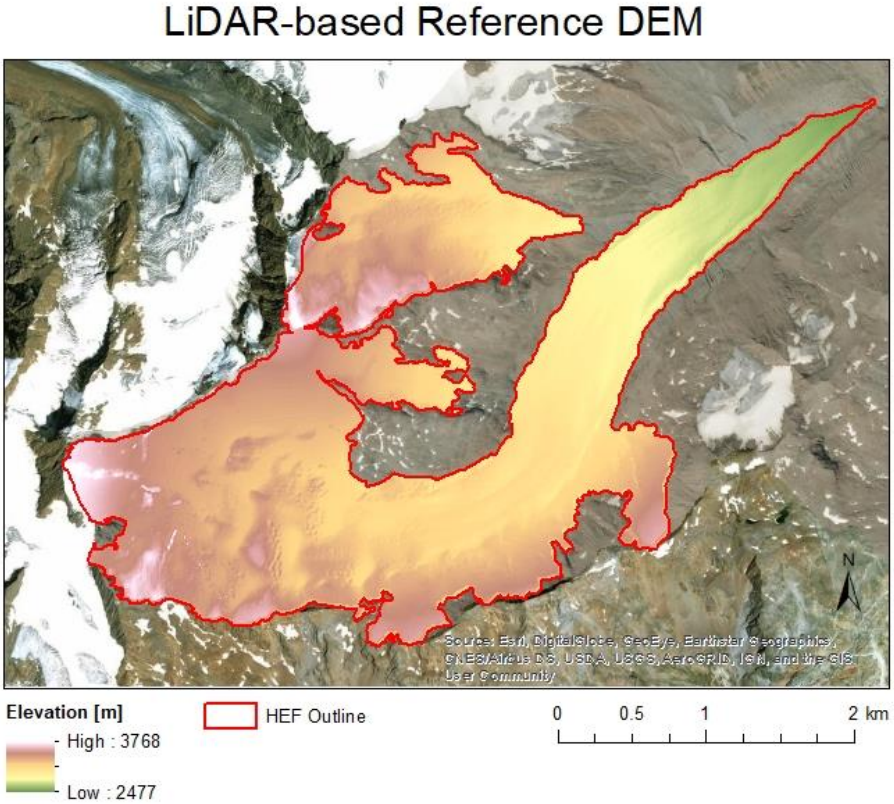

Figure 9. *Overview of the high-resolution LiDAR-based reference elevation data for the Hintereisferner.*

Frequency distributions in the form of a histogram and descriptive statistics are shown in Figures 10 and 11. The histograms of both the ASTER GDEM data and the LiDAR reference data show that elevation values around 3100 m are most frequent in the study area, although the bulk of the high-frequency elevation values tends to be a little bit more shifted towards the 3150-3200 m range in the reference data. In this regard, it should be noted that the maximum elevation values in the reference data are quite a bit higher than those in the ASTER GDEM data, although the local dip at around 2850 m is equally situated in both graphs. Moreover, the mean and standard deviation for the ASTER GDEM model and the LiDAR reference model are comparable, which indicates that the dispersion of the data is more or less the same for both models. It should be mentioned that, because the two cells with maximum elevation values differ 79 m and differences between corresponding individual cells for the two elevation models are sometimes even larger than 100 m, questions may arise about quality and suitability of the coarser ASTER GDEM elevation data. In many types of research, this aspect should not be ignored. In this study, however, this only plays a minor role because the primary focus is on methods of error quantification and not on the absolute accuracy of the error as such.

Another aspect that stands out in the graph of the ASTER GDEM data, is that a lot of fluctuation seems to be present in the frequency of the different elevation values for that model. This can be explained partly by the coarseness of the raster and partly by the precision of the data type, which cause a certain generalization of specific elevation values, resulting in higher frequencies for some elevation values (the steep peaks) right next to elevation values that are almost absent in the study area (the steep dips).

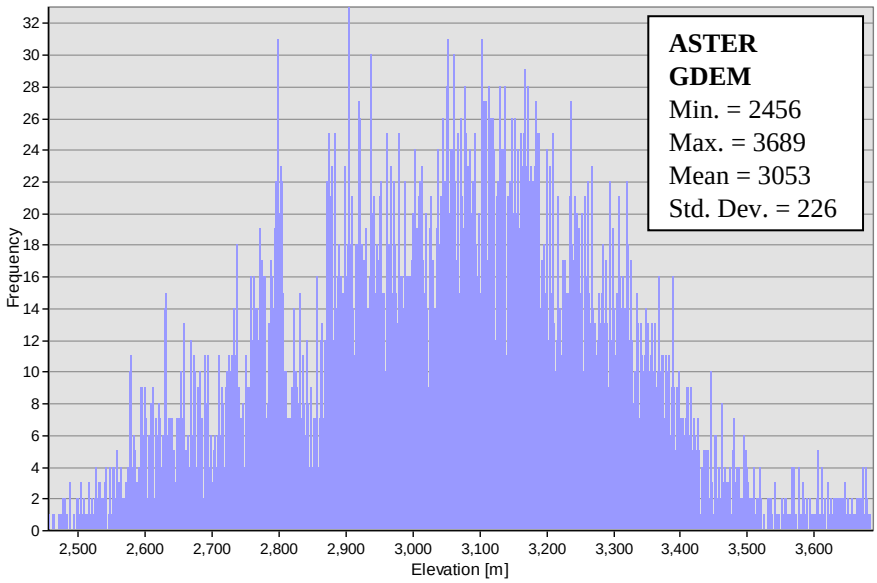

Figure 10. *Frequency distribution and descriptive statistics for the low-resolution ASTER GDEM elevation data.*

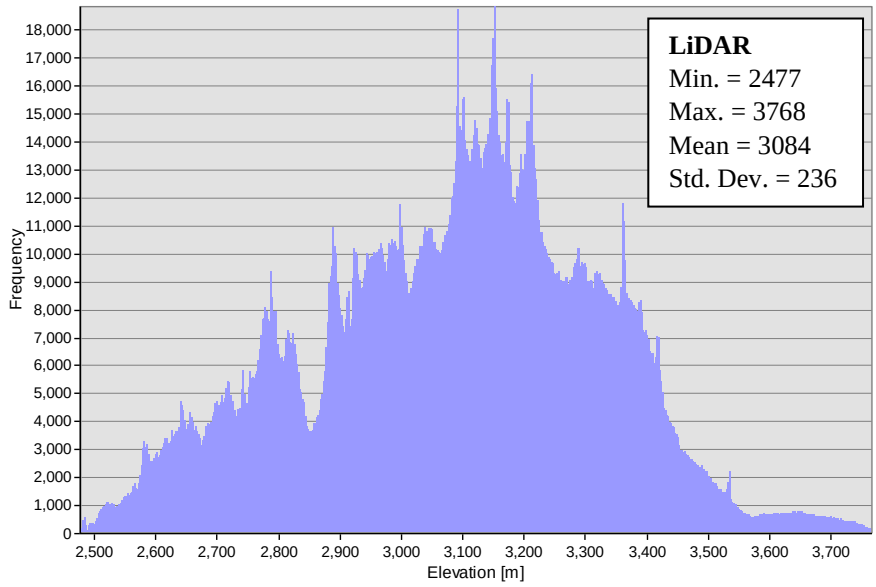

Figure 11. *Frequency distribution and descriptive statistics for the high-resolution LiDAR reference data.*

4.1.1 RMSE

Table 4 shows how the predicted values of the low-resolution data perform when compared against the reference data. In general, the lower the value for the root mean square error, the more accurate the model predicts the actual values. For the calculation of the RMSE, the total amount of available data points in the ASTER GDEM DEM (i.e. 11050, after NoValue records are removed) is sampled and compared against the LiDAR reference data.

Table 4. *Error quantification for the topographic parameter elevation, based on RMSE. The descriptive statistics in the table are based on the predicted values, i.e. the ASTER GDEM low-resolution data source.*

	Predicted	**Observed (reference)**	**Min.**	**Max.**	**Mean**	**RMSE**
Elevation	ASTER GDEM	LiDAR	2456 m	3689 m	3053 m	35 m

Because of the way the RMSE is calculated, this measure can be seen as an average magnitude of the error, which is expressed in the same units as the predicted data it refers to (i.e. the low-resolution ASTER GDEM data). It is therefore a very popular measure to quantify error in DEMs. However, as such, the RMSE is not very informative because it does not provide crucial information about the dispersion of the elevation data in the DEMs, nor gives it insight into the absolute values of the underlying errors. Because the errors are squared before they are averaged, a relatively large weight is given to the higher error values and RMSE increases quite a lot in cases of large error outliers. This is specifically true for outliers because RMSE does not necessarily increase proportionally with an increasing variance in the error values. In this respect, it is worth noting that outliers in error data, which often imply outliers in the underlying elevation data of one or both of the DEMs, are potentially false data that need to be excluded from the dataset. This is why reporting a single RMSE value has little meaning and should preferably be accompanied by descriptive statistics on the dispersion of the data of the elevation models that are compared, and the dispersion of the error values.

Moreover, the measure RMSE fails to acknowledge the spatial heterogeneity of error that is often present in DEMs. This shortcoming is illustrated by the selective sampling of data

points for the calculation of RMSE in Figure 12. The data points in the area that is depicted as Sample 1 yield an RMSE of roughly 12 m, whereas the RMSE based on Sample 2 is around 2 m.

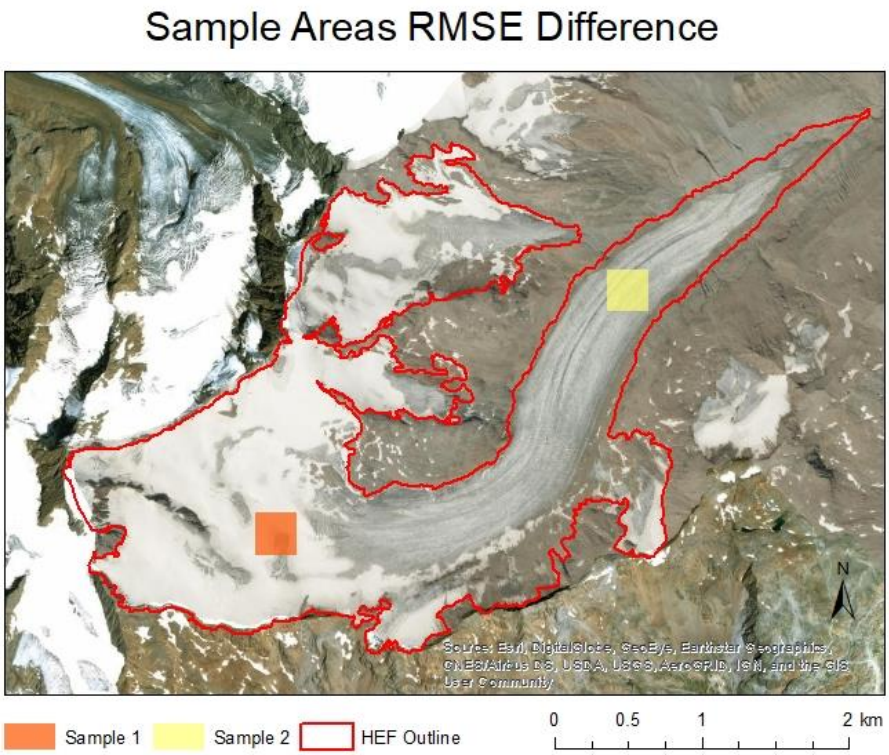

Figure 12. *The Hintereisferner glacier with two different sample areas to illustrate how a single RMSE value disregards spatial heterogeneity.*

As discussed in the introductory chapter of this thesis, knowledge about the spatial distribution of error in DEMs can be crucial in the process of determining suitable DEMs for specific research. This issue becomes even more relevant if geomorphological characteristics or topographical aspects in its broadest sense are key element of this research. As was mentioned earlier, error increases significantly when derived topographic parameters, such as slope or aspect, are compiled from elevation models.

4.2 Correlation analysis

Correlation analysis can be very helpful to gain more insight into the relation that may or may not exist between predicted and observed data. Inspection of a scatter plot, for instance, may be useful to support the abstract RMSE value that was calculated in the previous section and serves as an early warning system with regard to outliers in the data. Also, quantitative measures to express the strength and direction of a relationship, e.g. Pearson's r, tell the user of the DEMs in a very concise way something about the accuracy of the elevation data, although the RMSE has the advantage that it is expressed in the same unit as the data for which it was calculated.

For the correlation analysis, the amount of data points is restricted by an evenly distributed random sample grid to limit the output to a manageable size (Figure 13). The even distribution of the points ensures spatially unbiased sampling.

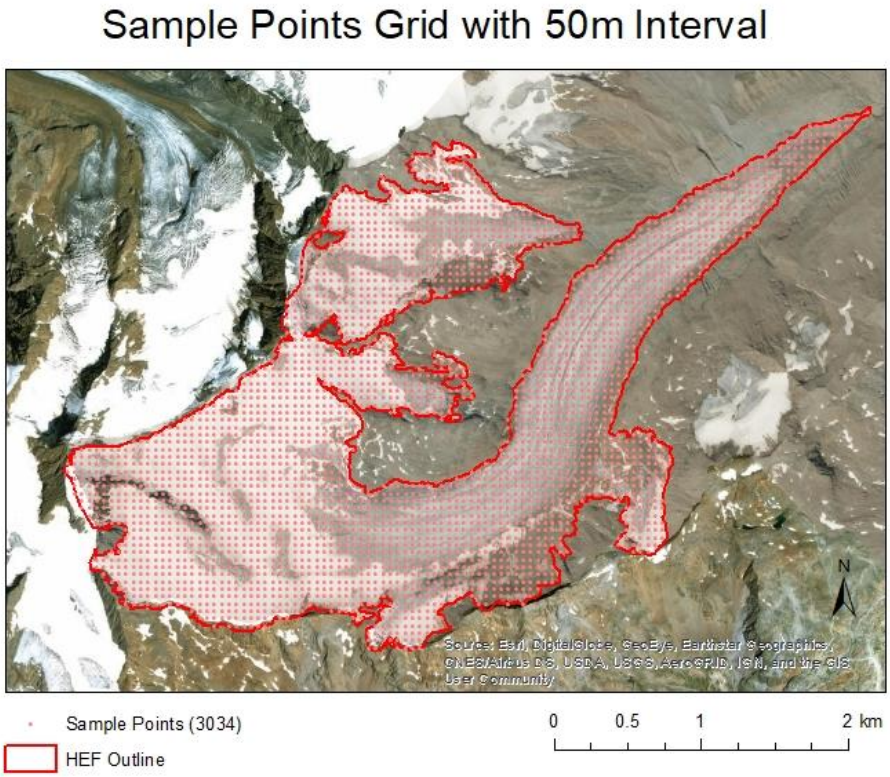

Figure 13. *Sample grid with 3034 sample points and 50 m interval to extract elevation values to compare for correlation analysis. NoValue samples are removed (these occur in the GDEM data due to the coarse resolution). Resulting number of samples: 2983.*

Figure 14a shows that the low-resolution ASTER GDEM elevation model has an almost perfect positive linear relationship with the high-resolution LiDAR reference model, with

the value for r being very close to +1.0. This comes as no surprise and is expected when comparing two DEMs for the same area with these ranges in the data. Within these large ranges, it is also hard to detect unexpected outliers that might or might not be present in the data. This approach makes clear that a correlation analysis for the whole dataset is very limited when it comes to quantifying or evaluating error in DEMs.

However, a correlation analysis, including outlier detection, may be useful to determine the level of agreement between observed and predicted data in DEMs if either the range of the data is altogether smaller, or if the focus of the analysis is on a certain (limited) elevation range. This could, for instance, be the case if one would like to know more about the level of agreement between the ASTER GDEM and LiDAR datasets for elevation levels between, say, 2000 and 2200 m. Or, alternatively, if the focus is on a specific part of the study area. To exemplify this, Figure 14b shows the level of agreement between the ASTER GDEM elevation model and the LiDAR reference model for a small part of the study area with relatively low elevation levels (sample 2 in Figure 12).

As was shown in the previous section, the RMSE value is rather sensitive to outliers in the data and without any form of outlier detection, it is impossible to determine to which extent the outliers affect this value, whereas with correlation analysis, one is able to estimate the influence of outliers. In addition, the correlation coefficient (in this case Pearson's r) instantly tells the user of the DEM something about the accuracy of the complete elevation model, albeit without a distinct reference framework since the interpretation of the outcome values for Pearson's r can be rather arbitrary. Absolute error values, on the other hand, are impossible to extract from just this correlation analysis. These error values would be represented by the difference between the predicted elevation values (i.e. the ASTER GDEM DEM) and their corresponding observed elevation values (i.e. the LiDAR reference DEM), something that cannot be derived from the correlation analysis directly. The residuals, which are expressed by the distances from the actual data points to the fitted line, are useless in this regard because the fitted line is, in this case of correlation analysis, not supposed to represent an estimation of an elevation model that best fits the input data.

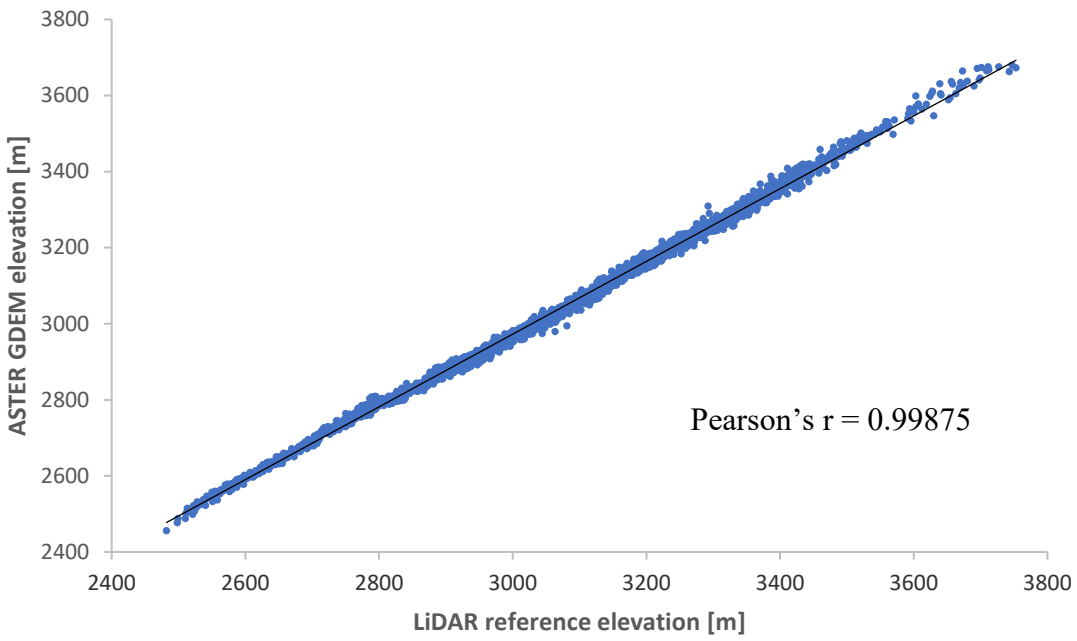

Figure 14a. *Correlation analysis for ASTER GDEM DEM versus the LiDAR reference DEM. The line is a best fit based on OLS and is added for visualization purposes.*

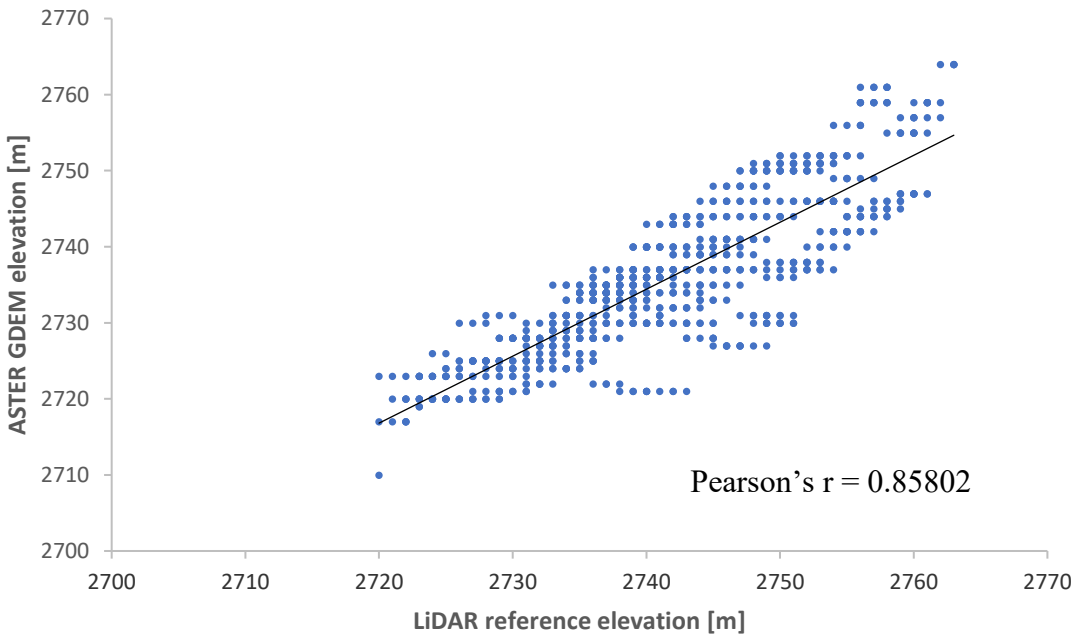

Figure 14b. *Correlation analysis for ASTER GDEM DEM versus the LiDAR reference DEM for a small part of the study area with relatively low elevation levels (sample 2 in Figure 12).*

4.3 Error Surfaces

The error surface in Figure 15 is a result of the subtraction of the high-resolution LiDAR reference elevation values from the corresponding low-resolution ASTER GDEM ones. The range of the values from the error surface provides useful information on the goodness of fit of the predicted elevation values (i.e. the ASTER GDEM): positive values in the error surface represent an overestimation of the actual elevation values, whereas the negative values correspond to an underestimation.

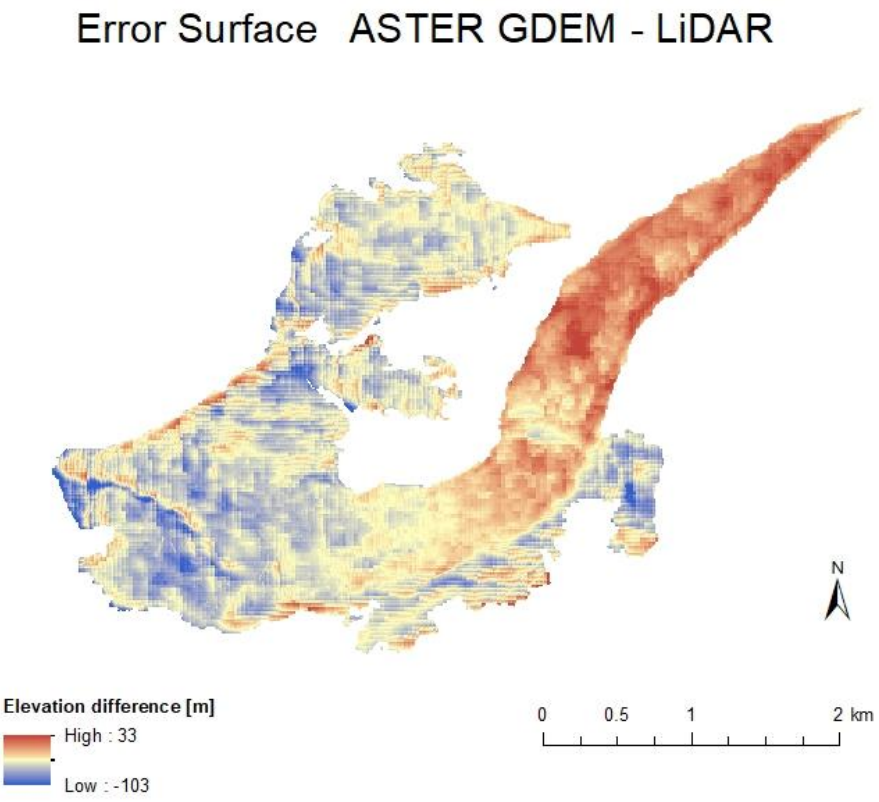

Figure 15. *The error surface is constructed by calculating the differences between the elevation values of the ASTER GDEM elevation model and the ones from the LiDAR reference elevation model. Both the high and low values in this error surface represent error, whereas an elevation difference of 0 would mean that the elevation value for that specific location is equal in both DEMs.*

Table 5 shows that, on average, the elevation values in the coarser ASTER GDEM-based DEM are underestimated. It also shows that the elevation difference data are rather dispersed, based on the standard deviation. This may be caused by the variation in topography of the study area, an aspect that is examined more closely in section 5.5.2 that deals with spatial resolution effects.

Table 5. *Descriptive statistics for the values of the elevation error surface, which is calculated by subtracting the reference data from the ASTER GDEM data.*

	Top. Parameter	Min.	Max.	Mean	Std. Dev.
Error Surface ASTER GDEM – LiDAR	Elevation	-103 m	33 m	-31 m	15 m

The histogram in Figure 16 shows that the frequency distribution of the error values is rather close to a normal distribution, albeit slightly right-skewed. The skewness is most likely caused by the significant amount of relatively low error differences that are concentrated in the areas with lower altitude at the north-eastern part of the Hintereisferner (compare Figures 8 and 9). An explanation for the mean and median within the range of negative values can be found in its relationship with the topography of the area (i.e. mainly high elevation values), which causes an overall underestimation within the ASTER GDEM (see Table 5).

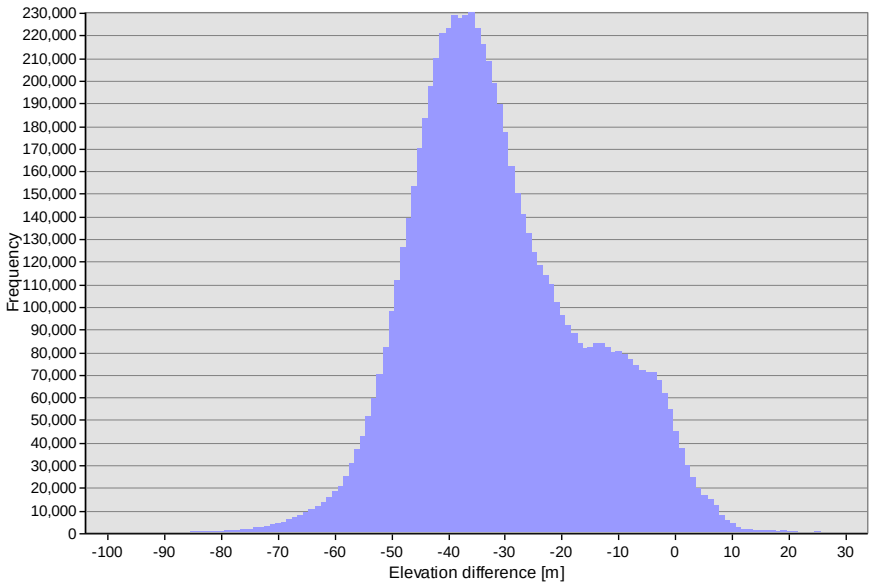

Figure 16. *Frequency distribution of the error values based on the ones that are depicted in Figure 15.*

Under- or overestimations are eliminated by creating an error surface with absolute values (see Figure 17). This alternative visualization provides a better insight into the actual derivation of the predicted ASTER GDEM values from the reference LiDAR data.

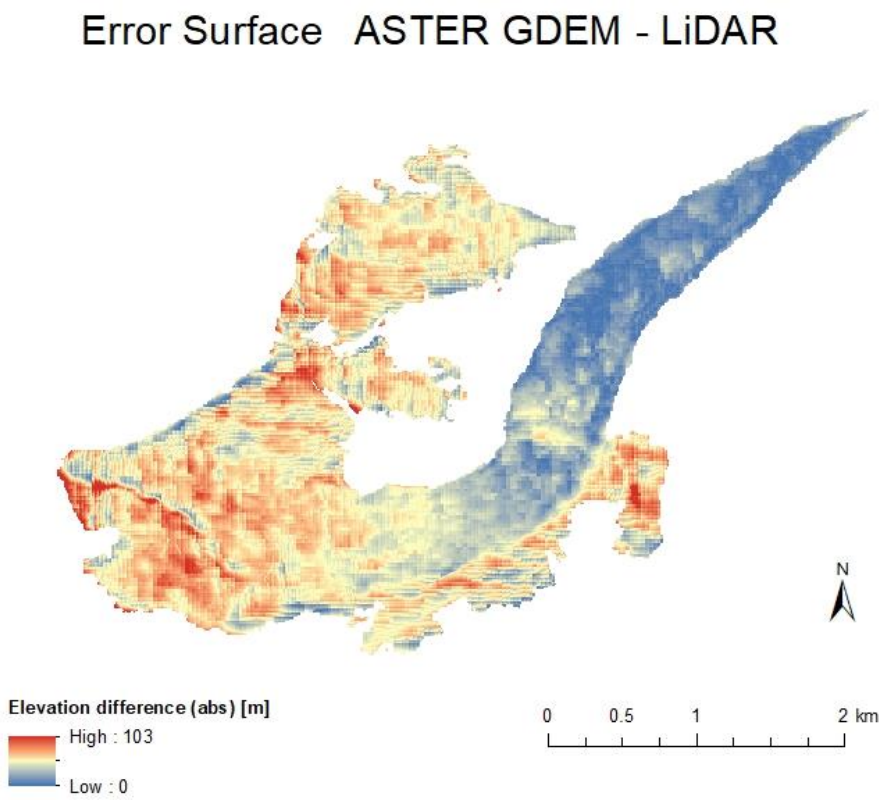

Figure 17. *Absolute elevation differences (i.e. error values) that result from comparison of the ASTER GDEM DEM with the LiDAR reference DEM.*

The error surfaces, both regular and with absolute values, are ideal for analysis of the spatial distribution of error in DEMs. For instance, one of the more notable things that can be observed when comparing Figure 17 to Figure 15, is that the overestimation of the predicted model, which is mainly concentrated in the relatively flat north-east part of the Hintereisferner with elevation levels at around 2500 m, turns out to be much smaller than the underestimation of the model, which is mainly situated at the more rugged terrain at the western part of the glacier. Another interesting point about the spatial distribution of error that stands out when looking at the error surface, is that the error in the DEM seems to relate to the topographical characteristics of the study area. For example, in the south western part of the Hintereisferner, a small line of high error values in NW-SE direction is present, right next to a line of very low error values (see Figure 17). When looking at the same location in the DEM itself, e.g. the one that is shown in Figure 9, a distinct topographical feature in the form of a ridge with an elevation of around 3700 m can be identified.

4.4 Measures of spatial autocorrelation and clustering

As the previous section made clear, the mapping of an error surface is purely a visualization technique to evaluate the spatial distribution of error in DEMs. The spatial patterns that emerge from this can also be quantified. To this end, several measures are calculated to analyze the spatial distribution or spatial patterning of those errors that were derived by calculating the error surface for the ASTER GDEM data. Because of the differences in approach and level of detail, the results are described in four subsections. The first two deal with the spatial distribution of error on a global level (i.e. the whole study area), whereas the last two show the resulting measures for the error distribution at a local level.

4.4.1 Global Moran's I

The calculated global Moran's I index comes with both a z-score and a p-value to evaluate its significance and interpret the result within the context of a null hypothesis (see Table 6). The null hypothesis states that the error values are randomly distributed among the study area (i.e. the error surface of the Hintereisferner). Based on the resulting z-score and p-value, this null hypothesis is rejected. The spatial distribution of high error values and/or low error values in the study area is more spatially clustered than would be expected if one assumes randomness. In fact, there is a less than 1% likelihood that this clustered pattern could be the result of random chance.

Table 6. *Global Moran's I index as a measure for spatial autocorrelation and clustering in the study area, based on a vectorized error surface.*

Moran's I	z-score	p-value
0.953	4036.515	0.000

The Global Moran's I measure may be useful if the user of a DEM wants to find out whether the errors in the elevation model are clustered, dispersed or distributed randomly throughout the entire model. The big advantage here, is that this spatial pattern is expressed in a single value, much like the RMSE expresses an "average error" in a single value. But, much like with the RMSE, the Global Moran's I measure also has the disadvantage that it tries to summarize for the whole study area with this single index value. This disregards the possibility that the spatial distribution has local anomalies, or at least the Global Moran's I index does not express this. Another disadvantage of the

Global Moran's I index, is that this value does not indicate whether the low error values, the high error values, or both are clustered. It just simply shows whether there is clustering, dispersion, or random distribution of data points.

4.4.2 Getis-Ord General G

The General G is used to measure the degree of clustering for either high values or low values. In this case, the clustering of high error values is of particular interest, although sometimes the user of a DEM might also want to know more about the spatial distribution of low error values in the model, e.g. to find out in which locations the data acquisition has been the most successful.

Table 7 shows the Getis-Ord General G index value, which is accompanied by a z-score and a p-value because it is an inferential statistic that needs to be interpreted within the context of a null hypothesis – just like Global Moran's I in the previous subsection. As was the case with Moran's I index, the Getis-Ord General G statistic also defines the null hypothesis as complete spatial randomness, which would mean that the error values are randomly distributed among the DEM. With a statistically significant p-value, the null hypothesis may be rejected. The positive z-score value indicates that the observed General G index value is larger than the expected one, which means the spatial distribution of the high error values in the dataset shows more spatial clustering than would be expected based on randomness. In fact, given the z-score of around 312, there is a less than 1% likelihood that this high-clustered pattern could be the result of random chance.

Table 7. *Getis-Ord General G as a measure for spatial autocorrelation and clustering in the study area, based on a vectorized error surface.*

Getis-Ord General G	z-score	p-value
0.000080	312.485813	0.000000

Reporting the Getis-Ord General G index value can be an improvement over the Global Moran's I value because it distinguishes between high-value and low-value clustering. This might aid the user of the DEM in determining whether or not improvement of the input data for the elevation model is desirable or required. Nevertheless, the General G index still lacks the ability to find specific locations with notably high error clustering. Another disadvantage of this method is that the algorithm with its spatial weights tends

to cancel out high and low values clusters, when both are more or less equally present in the study area (see section 4.4).

4.4.3 Local Moran's I

As the previous subsections on the quantification of spatial patterning of errors in DEMs showed, global measures can be useful indicators but are in need of additional information that sheds light upon the spatial location of error clustering.

The map in Figure 18 shows a visualization of Local Moran's I for the Hintereisferner glacier, based on the absolute error values. This Local Moran's I statistic enables both spatial outlier detection, as well as cluster analysis, based on significant hot or cold spots with a 95 percent confidence level.

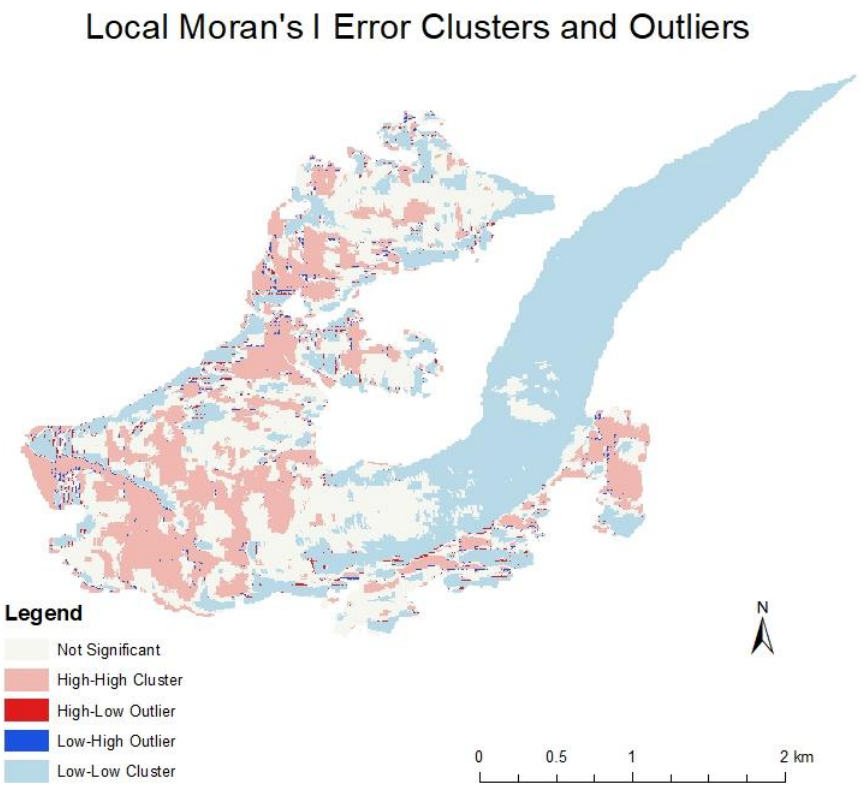

Figure 18. *Cluster and outlier detection based on Local Moran's I. Hot spot, cold spot and outlier mapping are based on a significance level of 95 percent.*

The results are categorized into clusters of high error values (high-high cluster), clusters of low error values (low-low cluster), spatial outliers with high values that are surrounded primarily by low values (high-low outlier), and spatial outliers with low values that are

surrounded primarily by high values (low-high outlier). This makes the (mapping of the) Local Moran's I statistic a very informative and suitable method to determine patterns in the spatial distribution of error in DEMs with the added bonus of spatial outlier detection. Presumably the biggest advantage of this method is that it enables the user of a DEM to specifically target error clusters and anomalies in the form of spatial outliers in order to improve the overall performance of the DEM. This method provides some very useful information on where to correct input data exactly or how to adjust the processing of raw data, for instance in case of interpolation flaws if the error clustering or spatial outliers are located in areas with scarce measurement points. It also specifically shows the location of the clustering of low errors, which can be useful to identify areas of the glacier that seem to have been measured more accurately.

*4.4.4 Getis-Ord Gi**

Another way of determining local clustering in the form of error hot or cold spots is by applying the Getis-Ord Gi* algorithm to the error data. The results for Hintereisferner glacier are mapped in Figure 19.

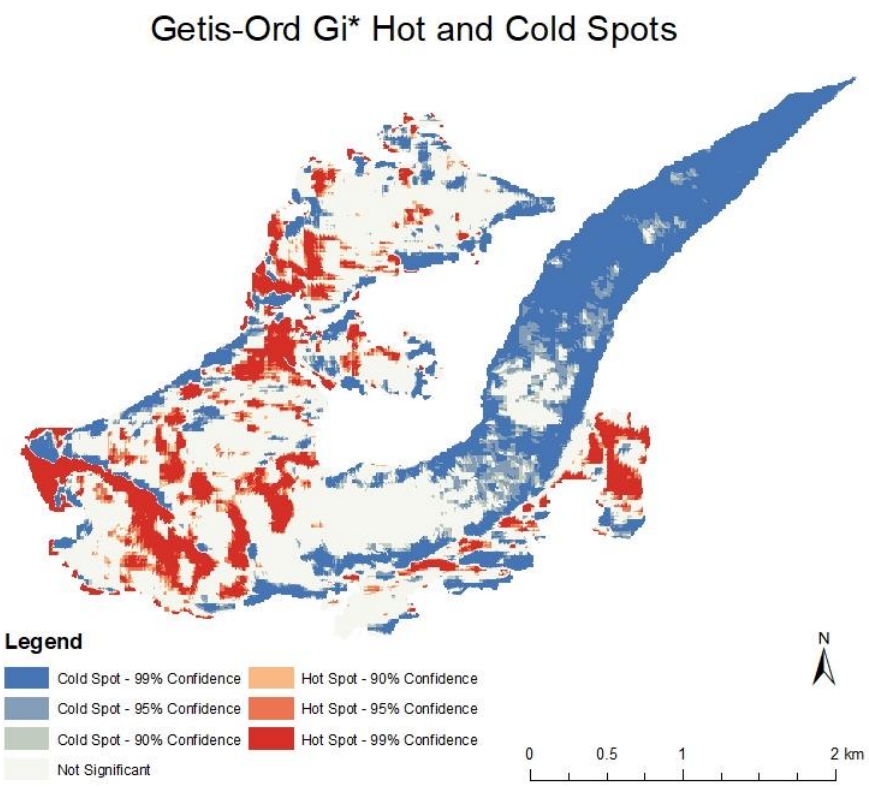

Figure 19. *Error hot spot and cold spot analysis based on the Getis-Ord Gi* statistic. Significant clustering is shown for different confidence levels.*

Getis-Ord Gi* and Local Moran's I differ in how they calculate spatial patterns. This becomes clear when looking at the north-eastern part of the study area where Local Moran's I yields only significant low error value clusters based on a 95 percent confidence level, whereas the clustering pattern based on the Getis-Ord Gi* statistic differentiates and also finds significant clustering that only upholds at a lower confidence level. Note that the Getis-Ord Gi* statistic does not allow for spatial outlier detection. In this regard, the Local Moran's I is the preferred measure.

A filter can be applied to extract useful information from the maps. The input data for the map in Figure 18, for example, can be divided into separate categories to show only the outliers or clusters, or even the specific types of outliers or clusters. Another possibility is to combine the error hot spot categories that are shown in Figure 19. This results in an expanded error map where also significant hot spots are shown that are selected based on a lower confidence level (see Figure 20). This could be a more appropriate map if the user of a DEM wants to make sure that potential error clusters that have a lower probability to be a statistically significant hot spot are also included for further quality inspection.

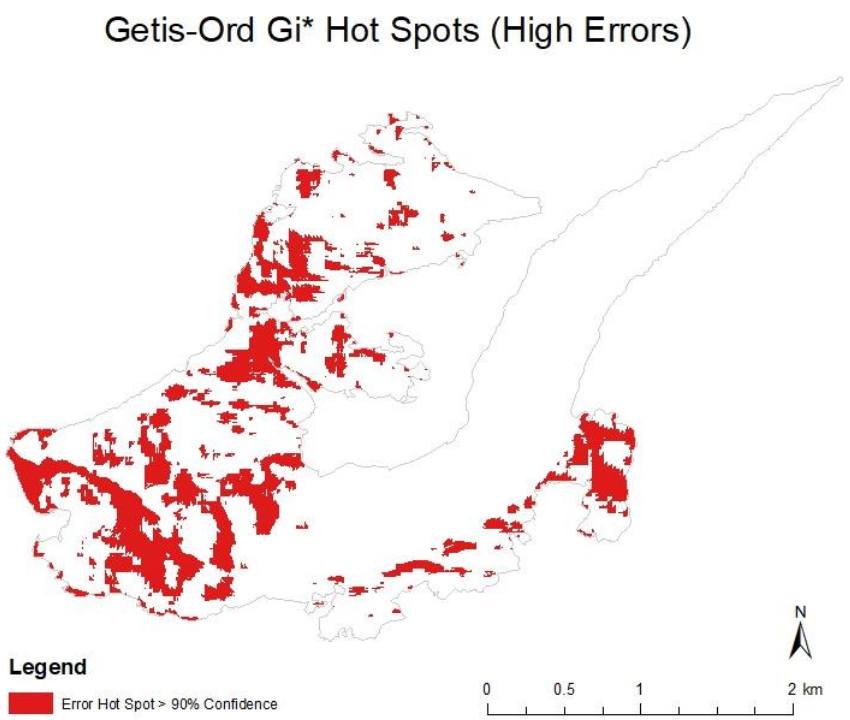

Figure 20. *Map of the filtered error hot spot analysis. All significant hot spots with a confidence level of 90 percent or higher are shown.*

4.5 Quantifying and evaluating major sources of error in DEMs

Thus far, the results and discussion have focussed on exploring methods to quantify and evaluate error and its spatial distribution in DEMs. As was discussed previously in the introductory chapter and the theoretical background, the sources where these errors stem from are categorized in roughly three different categories. Two of these major contributors to errors in DEMs are explored in more detail in the following subsections: interpolation effects and spatial resolution effects.

4.5.1 Interpolation effects

The map in Figure 21 shows the result of an interpolation based on kriging techniques. To assess whether or not this high-resolution version is an improvement over the original coarser ASTER GDEM data or results in increased error values, the interpolated DEM is compared to the LiDAR reference DEM (see Figure 22). The results give an indication of the effects that the interpolation might have on error values in the DEM.

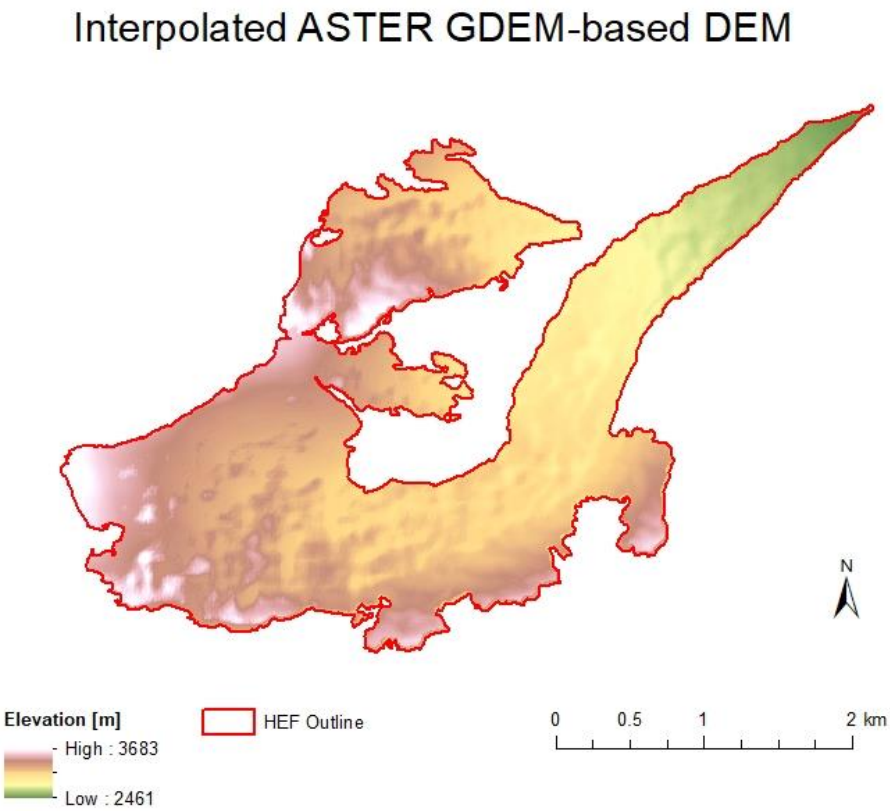

Figure 21. *An overview of the interpolated ASTER GDEM DEM of the Hintereisferner glacier. The low-resolution ASTER GDEM elevation model is interpolated to a high-resolution raster with 1 m cell size.*

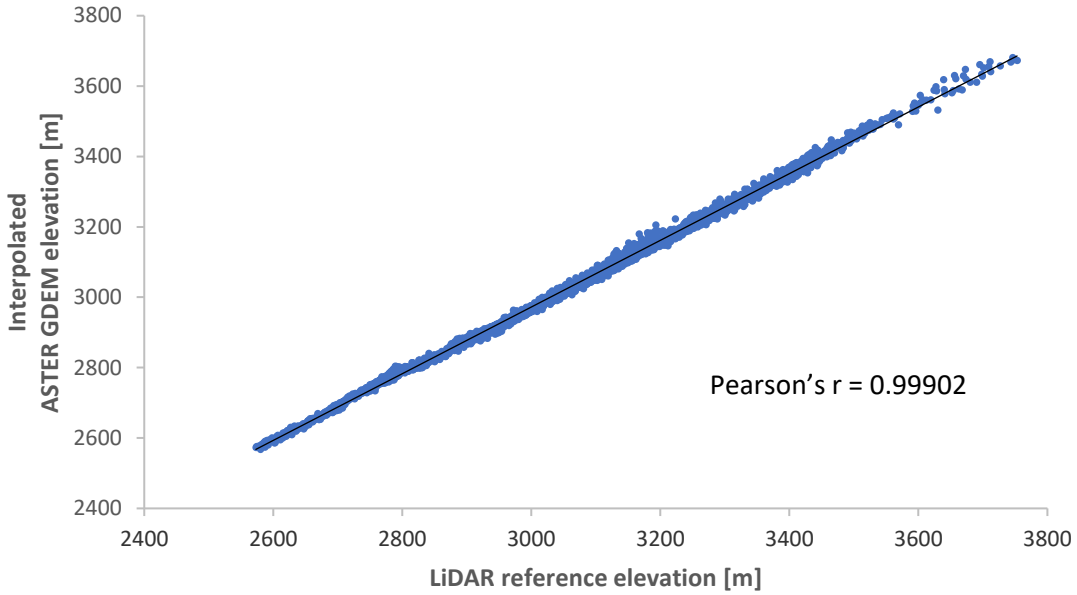

Figure 22. *Level of agreement between the interpolated DEM and the LiDAR reference DEM. The line is a best fit based on OLS and is for visualization purposes only.*

The scatterplot shows a nearly perfect positive relationship between the interpolated DEM and the reference data. This strong relationship is also expressed by a very high correlation coefficient. Compared to the correlation coefficient that was found by comparing the original low-resolution ASTER GDEM data with the LiDAR reference data, the coefficient is even slightly higher, although the difference is negligible. Table 8 provides an overview of the error quantification for the interpolated DEM, for which an RMSE was calculated.

Table 8. *Calculated RMSE for the interpolated DEM. The minimum, maximum and mean are based on the predicted values, i.e. the interpolated ASTER GDEM data.*

	Predicted	**Observed (reference)**	**Min.**	**Max.**	**Mean**	**RMSE**
Elevation	Interpolated ASTER GDEM	LiDAR	2461 m	3683 m	3052 m	36 m

In comparison to the original coarse ASTER GDEM DEM, applying the interpolation shows almost no increase or decline in error values. Both Pearson's r and RMSE are

comparable and the changes in the range and dispersion of elevation values are minimal. It means that the kriging interpolation had virtually no effect on the quality of the DEM. This can be very valuable knowledge to the user of the DEM because it means that, under these specific conditions, interpolation effects can be ruled out as a major source of error in the DEM. It also means that the use of the original, non-interpolated data may suffice. This can be different, however, if the elevation model is used to compile derived topographic parameters. As was described in the chapter on data and methods, these derived parameters tend to be more susceptible to small changes in elevation values in the input data and might therefore manifest a stronger deviation from the original data.

4.5.2 Spatial resolution effects

Another major source of error in DEMs is the spatial resolution and the effect it has on the level of detail that is captured in the DEM. Section 2.6.3 gives an in-depth description of these spatial resolution effects. To estimate the influence of spatial resolution on the error values within the DEM, the slope as a derived topographic parameter is calculated and used as a proxy for large elevation changes within a relatively small spatial extent. The potential of determining spatial resolution effects with the aid of slope as a proxy is explained in section 4.4.2.

Determining the scope of spatial resolution effects in DEMs is potentially very useful to gain a better understanding of the underlying factors that are causing the errors in DEMs. If the user of a DEM is able to estimate the influence of spatial resolution effects and combine this with an estimation of the influence of interpolation effects, as was shown in the previous section, then this would already isolate the larger part of two of the three major categories of error sources in DEMs.

The mapped slope values for the high-resolution reference DEM are shown in Figure 23. They are divided into classes of 10 degrees each. By comparing these slope values with the elevation differences (i.e. the error values) from the error surface that was previously calculated, a first impression is given of a possible correlation between the two (see Figure 24 for an overview of both maps).

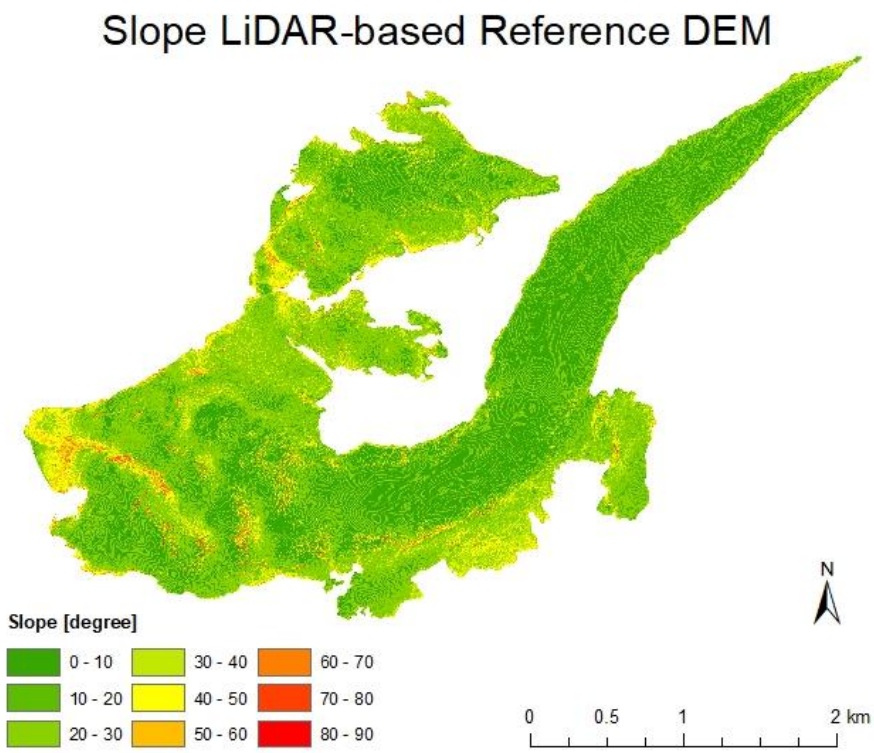

Figure 23. *Mapped slope values for the LiDAR reference data. The slope values are calculated on the level of individual cells in the raster and then reclassified.*

Figure 24 clearly shows that the highest slope values in the study area coincide with the highest error values in the DEM, especially in the southern and western part of the Hintereisferner glacier. However, it also shows that, besides these locations with high error values, there are many areas in the DEM that have high error values that do not match with high slope values. These areas are particularly prominent in the western part of the study area, where the highest error values sometimes even overlap with almost flat areas. To find out more about the partial mismatch between error values and slope, a correlation analysis is performed. The scatterplot in Figure 25 shows that there is hardly any relationship detectable if one looks at the data for the whole study area. But, more importantly, the graph also shows that slope values tend to cluster around specific values. This is due to scaling problems, which limit the level of detail in the calculation of the slope values. Nevertheless, if spatial resolution effects would be a significant factor of influence, the plotted error values would be a lot closer to the fitted line curve.

Because the southern and western parts of the study area generally have the highest elevation values (compare Figure 9), this seems to indicate that error in the DEM positively correlates with elevation levels but not necessarily exclusively with

characteristics of the land surface that are susceptible to spatial resolution effects. This leaves room for speculation on what causes these large error values in areas that show little variation in topography. For instance, high elevation values in general could be problematic for the ASTER GDEM data acquisition, or differences in land cover could significantly influence measurements (e.g. the amount of snow cover, indications for which can be found in Figure 6c).

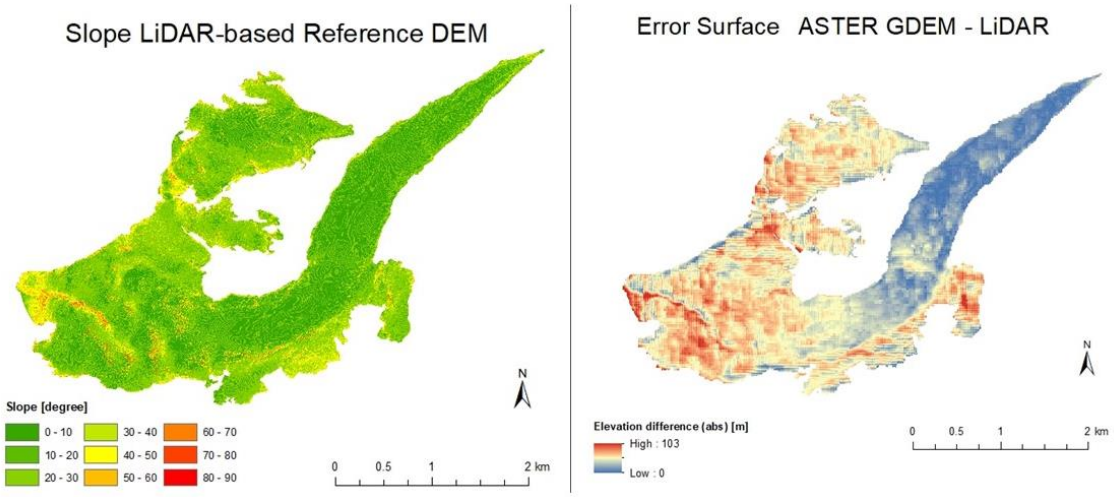

Figure 24. *Comparison of slope values against elevation differences (i.e. error values) for the whole study area.*

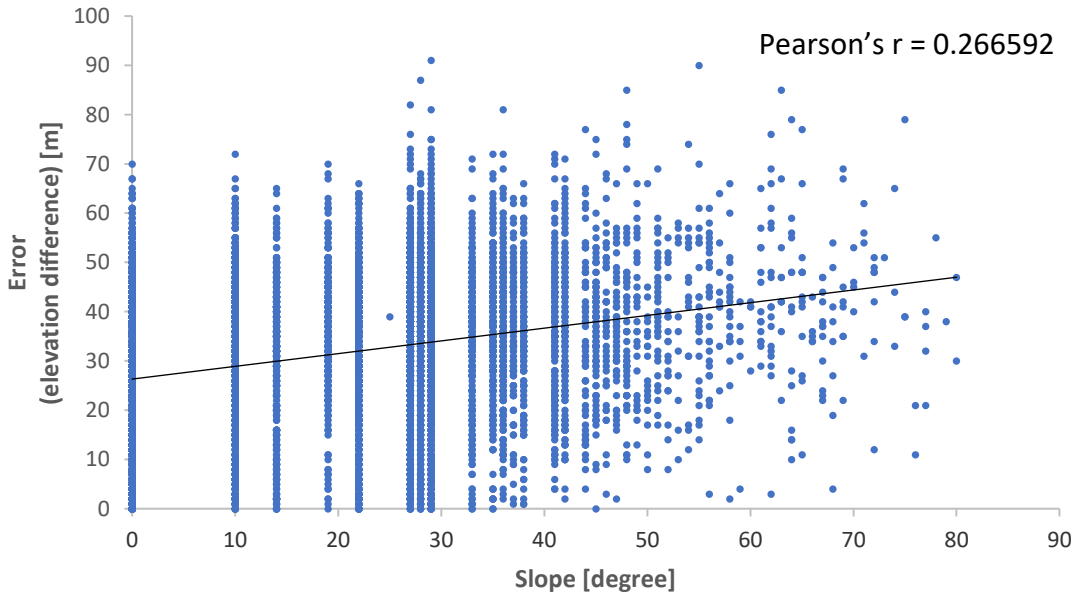

Figure 25. *Level of agreement between the error values and slope values to determine the influence of spatial resolution effects.*

4.6 Caveats and limitations

In order to correctly evaluate the results and conclusions of this study, certain caveats and limitations have to be mentioned:

- Bias: Analysis of remote sensing data generally requires a mix of technical data analysis and expert judgment. Both components can be subject to (systematic) bias. Please be aware that identification and/or reduction of bias have not been part of the data handling, nor has any distinction been made by differences in land cover, weather conditions or type of sensor (e.g. with regard to the ability to penetrate clouds or snow or ice to a certain depth). The reader should bear in mind that in this respect margins of error were not included in the results or accounted for in the methods of quantification and evaluation of error.
- Spatial accuracy: Each acquisition of remote sensing data has its own flaws when it comes to (spatial) accuracy. Because the main factor in this study concerned the exploration of methods, the focus has been on vertical accuracy and not on horizontal accuracy (although this would obviously matter if accurate elevation values were required).
- Temporal resolution: Due to restrictions in data availability, the comparisons for the error quantifications had to be made based on datasets from 4 and 17 October 2011 respectively. Seasonal variations in snow or ice cover are therefore not included in the analyses, although this aspect might have been able to explain discrepancies found in the estimation of spatial resolution effects.
- Reference data: In order to conduct most of the error quantifications and evaluations in this study, reference data of high precision and accuracy is required. In other studies, this is not always readily available, for obvious reasons. On the contrary, if high-quality elevation data is available, this would naturally be used as input data for the DEM instead. Nevertheless, by showing how the methods of error quantification work that were explored in this study, estimations can be made with regard to the scope of error in DEMs for similar contexts.

5. CONCLUSIONS AND RECOMMENDATIONS

This study explores methods to quantify and evaluate error in digital elevation models built from remotely sensed elevation data of the Hintereisferner glacier. A special focus lies on glacier surfaces because glaciers are often inaccessible for field observations but in the same time prone to measurement errors. They would therefore particularly benefit from a comprehensive error assessment. One of the primary aspects of the study is to find suitable methods that also include the spatial distribution of error because this is generally a somewhat neglected part of quality assessment of DEMs, although it potentially has a significant impact on the way DEMs are used in research, especially if geomorphological or topographical aspects are part of this. In addition to identifying and discussing methods to quantify and evaluate existing errors in DEMs, this study also looks at some major sources from which the errors stem to find out if the influence of these sources on the resulting errors can be estimated. To this end, two out of three major categories of error sources were selected: interpolation effects and spatial resolution effects.

The explored methods are chosen based on the relevant scientific literature on quality assessment of DEMs. They include quantitative error measures, such as RMSE, but also more evaluative approaches, such as correlation analysis. The results of the calculation of RMSE for the study area confirmed that, as such, the RMSE as a single value is limited in its capability to explain both the variation and dispersion in the error values. This is in line with findings in similar studies that focus on the quality of DEMs, as was pointed out before in the introduction and theory. RMSE also fails to give an indication as to how large the errors in the elevation model are on a local scale, nor does it inform the user of the DEM where errors are located within the model or how they are distributed. This is, of course, inherent in these global measures of error. Nevertheless, considering the importance of knowledge on the spatial distribution of error, especially when dealing with DEMs, the single RMSE value that is so often used with regard to quantifying error in DEMs, seems to be a somewhat poor choice.

As an alternative to calculating the RMSE, error in DEMs can also be quantified and evaluated by performing a correlation analysis. The results from this method show that plotting the original DEM values against very accurate reference data gives the user of a DEM a fairly good impression of the overall level of agreement of the data, i.e. the

accuracy of the input DEM. This way of visualizing the elevation data also serves as an early warning system with regard to outliers in the data, which is especially helpful if the correlation analysis is performed in combination with the calculation an RMSE value since this value is rather sensitive to outliers in the data. In addition to the scatterplot, the correlation coefficient (in this case Pearson's r) can be calculated. This quantitative measure instantly tells the user of the DEM something about the accuracy of the complete elevation model, albeit without a distinct reference framework since the interpretation of the outcome values for Pearson's r can be rather arbitrary. One of the disadvantages of performing a correlation analysis to quantify and evaluate error in DEMs is the fact that absolute error values are impossible to extract from the scatterplot and the correlation coefficient. Also - like with the calculation of an RMSE value - spatial distribution of error is not part of this method.

Including spatial distribution as part of the quantification and evaluation of error in DEMs is done by exploring methods like the creation of error surfaces or approaches that quantify the spatial patterning of error values in DEMs. Error surfaces offer a useful combination of quantification and evaluation of both error and its spatial distribution: absolute error values are shown, and their spatial distribution is observable. The range of the values from the error surface provides insight into the goodness of fit of the predicted elevation values (i.e. the ASTER GDEM): positive values in the error surface represent an overestimation of the actual elevation values, whereas the negative values correspond to an underestimation. Furthermore, a direct comparison between error surfaces and the elevation models themselves, allow the user of the DEMs to link error to topographical characteristics within the study area. In the case of the Hintereisferner glacier, this resulted in a clear overlap between high error values and distinct topographical features, such as ridges or crevasses.

The introduction and methodology part of this thesis have made clear that a comprehensive error quantification and evaluation requires the inclusion of spatial patterning of the error values throughout the DEM. Creating error surfaces is a very straightforward way to do this but lacks a proper quantification of this aspect because it is merely a visualization technique. To quantify the spatial patterns, e.g. clustering, that emerge from error surfaces, several measures of spatial autocorrelation or clustering are calculated. Two of them are global and cover the study area as a whole: Global Moran's

I and Getis-Ord General G. The other two are local and consider variation in clustering of the error values within the study area: Local Moran's I and Getis-Ord Gi*. The results show that the issue of global versus local approach is rather essential in choosing a suitable method to quantify and evaluate spatial distribution of error in DEMs. The fact that both the global measures try to summarize for the whole study area with a single index value is quite a disadvantage and would restrict the user of a DEM in its aim to improve the quality of a DEM not only by looking at absolute error values, but also by looking at spatial clustering or spatial anomalies to identify weaknesses in the elevation model, which are, as the results show, often of a local nature. Therefore, the local measures of error clustering are preferred. In this respect, the Local Moran's I is favored over the Getis-Ord Gi* because the Local Moran's I allows for spatial outlier detection, something that is potentially very useful to the user of the DEM because it often indicates anomalies in the data (like the 'regular' outliers in the elevation data or error values).

In light of the above, it can be concluded that:

- Suitable methods for error quantification and evaluation include calculating an RMSE value, performing correlation analysis, and calculating error surfaces and measures of spatial autocorrelation or clustering;
- Quantifying error in a DEM by calculating an RMSE value is probably the most convenient and straight-forward way. But without proper context, a single RMSE error can not show or explain dispersion in elevation values. Moreover, this study made explicit that absence of the spatial component makes a single RMSE value a poor choice when quantifying error in DEMs because this aspect is essential due to the spatial nature of the data in DEMs;
- Correlation analysis turns out to be the weaker choice to quantify and evaluate error in DEMs in this study, both in terms of the absolute error and its spatial distribution;
- Error surfaces are presumably the most powerful methods in this specific study to gain insight into both the absolute error values and the spatial distribution of them. They are easy to understand, and they provide the user of a DEM with adequate information, although they lack quantitative measures that report the error term or its spatial pattern in the DEM with a single number;
- Calculation of local measures of error clustering that include spatial outlier detection (e.g. Local Moran's I) is a valuable addition to the common approach of error

quantification and evaluation for DEMs. Especially if the elevation data is used in cases where spatial clustering of error would increase the total error in the resulting output.

As a last step in this thesis, two of the major sources of error in DEMs – interpolation effects and spatial resolution effects - are explored to find methods to quantify and evaluate their influence on the resulting error values. To estimate interpolation effects, a comparison is made between the error values that resulted from the original ASTER GDEM data and the ones that were calculated based on the interpolated ASTER GDEM data. The comparison is based on correlation analysis, including a correlation coefficient, and RMSE because these measures of error should suffice to give the user of the DEM at least a rough idea about the effects the interpolation had on data quality. Results show that both the correlation coefficient and the RMSE are comparable in both cases. There is hardly a noticeable increase or decrease in error values due to the interpolation, which leads to the conclusion that, in this case, the interpolation had virtually no effect on the quality of the DEM. Although it should be noted that this very specific case contradicts general findings in the scientific literature on this topic (see section 2.6).

The estimation of spatial resolution effects is based on the compilation of a derived topographic parameter, i.e. slope. Slope serves as a proxy for abrupt elevation changes on a small spatial extent and is therefore an ideal parameter to compare to the error data in order to find out if there is a relationship between the two. If a strong correlation between slope values and error values is found, then this would be an indicator for the influence of spatial resolution effects on the error of the DEM. In this case, the results showed that the highest slope values in the study area coincide with the highest error values in the DEM, especially in the southern and western part of the Hintereisferner glacier. However, the results also show that, besides these locations with high error values, there are many areas in the DEM that have high error values that do not match with high slope values. This leaves room for speculation on what causes these large error values in areas that show little variation in topography. Regardless, both the approaches on estimating interpolation effects and spatial resolution effects lead to the conclusion that, in this case, these two major sources of error have, in fact, relatively little influence on the error values in the DEM.

Recommendations for further study include:

- Applying the chosen methods of quantifying an evaluating error and its spatial distribution on different data sources with different resolutions and different remote sensing devices to find an optimum.
- Inclusion of different study areas to be able to distinguish results for various types of glaciers and/or glacial surfaces (e.g. debris cover and type of snow or ice). This seems particularly interesting since the results in this study showed a rather unexpected relationship between high error values and relatively flat topography for some parts of the study area, something that might be explained by the type of land cover. Variation in temporal resolution could be an option as well.

REFERENCES

ALI, T., MEHRABIAN, A. (2009) A novel computational paradigm for creating a Triangular Irregular Network (TIN) from LiDAR data, *Nonlinear Analysis*, **71**(12), 624-629.

ANSELIN, L. (1995) Local indicators of spatial association – LISA, *Geographical Analysis*, 27, 93-115.

ARNOLD, N.S., REES, W.G., HODSON, A.J., KOHLER, J. (2006a) Topographic controls on the surface energy balance of a high Arctic valley glacier, *Journal of Geophysical Research*, 111, F02011.

ARNOLD, N.S., REES, W.G., DEVEREUX, B.J., AMABLE, G.S. (2006b) Evaluating the potential of high-resolution airborne LiDAR data in glaciology, *International Journal of Remote Sensing*, **27**(6), 1233-1251.

BAMBER, J.L., RIVERA, A. (2007) A review of remote sensing methods for glacier mass balance determination, *Global and Planetary Change*, 59, 138-148.

BATER, C.W., COOPS, N.C. (2009) Evaluating error associated with lidar-derived DEM interpolation, *Computers & Geosciences*, 35, 289-300.

BRAUN, A., FOTOPOULOS, G. (2007) Assessment of SRTM, ICESat, and survey control monument elevations in Canada, *Photogrammetric Engineering & Remote Sensing*, **73**(12), 1333-1342.

BURGMANN, R., ROSEN, P.A., FIELDING, E.J. (2000) Synthetic aperture radar interferometry to measure Earth's surface topography and its deformation, *Annual Review of Earth and Planetary Sciences*, 28, 169-209.

CARLISLE, B.H. (2005) Modelling the Spatial Distribution of DEM Error, *Transactions in GIS*, **9**(4), 521-540.

CHANG, K., TSAI, B. (1991) The effect of DEM resolution on slope and aspect mapping, *Cartography and Geographic Information Systems*, 18, 69-77.

CHEN, Y., ZHOU, Q. (2013) A scale-adaptive DEM for multi-scale terrain analysis, *International Journal of Geographical Information Science*, **27**(7), 1329-1348.

CHOW, T.E., HODGSEN, M.E. (2009) Effects of lidar post-spacing and DEM resolution to mean slope estimation, *International Journal of Geographical Information Science*, **23**(10), 1277-1295.

CLARKE, G.K.C. (1991) Length, width and slope influences on glacier surging, *Journal of Glaciology*, **37**(126), 236-246.

ERDOGAN, S. (2010) Modelling the spatial distribution of DEM error with geographically weighted regression: An experimental study, *Computers & Geosciences*, 36, 34-43.

ETZELMÜLLER, B. (2000) On the quantification of surface changes using grid-based digital elevation models (DEMs), *Transactions in GIS*, **4**(2), 129–143.

ETZELMÜLLER, B., BJÖRNSSON, H. (2000) Map analysis techniques for glaciological applications, *International Journal of Geographical Information Science*, **14**(6), 567–581.

FELIKSON, D., BARTHOLOMAUS, T.C., CATANIA, G.A., KORSGAARD, N.J., KJÆR, K.H., MORLIGHEM, M., NOËL, B., VAN DEN BROEKE, M., STEARNS, L.A., SHROYER, E.L., SUTHERLAND, D.A., NASH, J.D. (2017) Inland thinning on the Greenland ice sheet controlled by outlet glacier geometry, *Nature Geoscience*, 10, 366-371.

FERRETTI, A., MONTI-GUARNIERI, A., PRATI, C., ROCCA, F. MASSONNET, D. (2007) InSAR Principles: Guidelines for SAR Interferometry Processing and Interpretation (TM-19, February 2007), *InSAR Principles*, ESA Publications: Noordwijk.

FISCHER, A. (submitter/analyst) (2012) GLIMS Glacier Database, Boulder, CO, National Snow and Ice Data Center, http://dx.doi.org/10.7265/N5V98602.

FISHER, P.F., TATE, N.J. (2006) Causes and consequences of error in digital elevation models, *Progress in Physical Geography*, **30**(4), 467-489.

FUJISADA, H., BAILEY, G.B., KELLY, G.C., HARA, S., ABRAMS, M.J. (2005) ASTER DEM performance, *IEEE Transactions on Geoscience and Remote Sensing*, **43**(12), 2707–2714.

GAO, J. (1997) Resolution and accuracy of terrain representation by grid DEMs at a micro-scale, *International Journal of Geographic Information Science*, 11, 199–212.

GAO, J., LIU, Y. (2001) Applications of remote sensing, GIS and GPS in glaciology: a review, *Progress in Physical Geography* **25**(4), 520–540.

GARDELLE, J., BERTHIER, E., ARNAUD, Y. (2012) Impact of resolution and radar penetration on glacier elevation changes computed from DEM differencing, *Journal of Glaciology*, **58**(208), 419-422.

GÄRTNER-ROER, I., NAEGELI, K., HUSS, M., KNECHT, T., MACHGUTH, H., ZEMP, M. (2014) A database of worldwide glacier thickness observations, *Global and Planetary Change*, 122, 330-344.

GOERLICH, F., BOLCH, T., MUKHERJEE, K., PIECZONKA, T. (2017) Glacier Mass Loss during the 1960s and 1970s in the Ak-Shirak Range (Kyrgyzstan) from Multiple Stereoscopic Corona and Hexagon Imagery, *Remote Sensing*, **9**(275), 1-18.

GONGA-SAHOLIARILIVA, N., GUNNELL, Y., PETIT, C., MERING, C. (2011) Techniques for quantifying the accuracy of gridded elevation models and for mapping uncertainty in digital terrain analysis, *Progress in Physical Geography*, **35**(6), 739-764.

GOODCHILD M.F., BUTTENFIELD B.P., WOOD, J. (1994) Introduction to visualizing data quality, in: Hearshaw, H.M., Unwin, D.J. (eds.) Visualization in Geographic Information Systems, New York: John Wiley and Sons, 141-149.

GRATTON, D.J., HOWARTH, P.J., MARCEAU, D.J. (1990) Combining DEM parameters with Landsat MSS and TM imagery in a GIS for mountain glacier characterization, *IEEE Transactions on Geoscience and Remote Sensing*, **28**(4), 766–769.

HANSSEN, R.F. (2001) Radar Interferometry, Vol. 2 of Remote Sensing and Digital Image Processing, Springer Netherlands: Dordrecht.

HASAN, A., PILESJÖ, P., PERSSON, A. (2012) On generating digital elevation models from LiDAR data – resolution versus accuracy and topographic wetness index indices in northern peatlands, *Geodesy and Cartography*, **38**(2), 57-69.

HEBELER, F., PURVES, R.S. (2009) The influence of elevation uncertainty on derivation of topographic indices, *Geomorphology*, 111, 4-16.

HIRANO, A., WELCH, R., LANG, H. (2003) Mapping from ASTER stereo image data: DEM validation and accuracy assessment, *ISPRS Journal of Photogrammetry &Remote Sensing*, 57, 356-370.

HUNTER, G.J., CAETANO M., GOODCHILD, M.F. (1995) A methodology for reporting uncertainty in spatial database products, *Journal of the Urban and Regional Information Systems Association*, 7, 11-21.

JAMES, W.H.M., CARRIVICK, J.L. (2016) Automated modelling of spatially-distributed glacier ice thickness and volume, *Computers & Geosciences*, 92, 90-103.

JOERG, P.C., MORSDORF, F., ZEMP, M. (2012) Uncertainty assessment of multi-temporal airborne laser scanning data: A case study on an Alpine glacier, *Remote Sensing of Environment*, 127, 118-129.

KÄÄB, A., PAUL, F., MAISCH, M., HOELZLE, M., HAEBERLI, W. (2002) The new remote sensing-derived Swiss glacier inventory: II. First results, *Annals of Glaciology*, 34, 362–366.

KÄÄB, A., HUGGEL, C., FISCHER, L., GUEX, S., PAUL, F., ROER, I., SALZMANN, N., SCHLAEFLI, S., SCHMUTZ, K., SCHNEIDER, D. (2005) Remote sensing of glacier- and permafrost-related hazards in high mountains: an overview, *Natural Hazards and Earth System Sciences*, 5, 527-554.

KÄÄB, A. (2010) Aerial Photogrammetry in glacier studies, in: Pellikka, P., Rees, W.G. (eds.) Remote sensing of glaciers: techniques for topographic, spatial, and thematic mapping of glaciers, Leiden: CRC Press, pp. 115-137.

KÄÄB, A., WINSVOLD, S.H., ALTENA, B., NUTH, C., NAGLER, T., WUITE, J. (2016) Glacier Remote Sensing Using Sentinel-2. Part I: Radiometric and Geometric Performance, and Application to Ice Velocity, *Remote Sensing*, **8**(598), 1-24.

KAMB, B. (1987) Glacier surge mechanism based on linked cavity configuration of the basal water conduit system, *Journal of Geophysical Research*, **92**(B9), 9083-9100.

KHORRAM, S., KOCH, F.H., VAN DER WIELE, C.F., NELSON, S.A.C. (2012) Remote Sensing (Springer Briefs in Space Development, series ed. Pelton, J.N.), Heidelberg: Springer Verlag.

KIM, H. (2014) Sensitivity of vegetation indices to spatial degradation of RapidEye imagery for paddy rice detection: a case study of South Korea, *GIScience & Remote Sensing*, **51**(1), 1-17.

KOMAR, G. (2017) Technology advancement and challenges in spaceborne Lidar for earth science, *IEEE International Geoscience and Remote Sensing Symposium (IGARSS)*, Fort Worth, TX, 4208-4211.

LE BRIS, R., PAUL, F. (2013) An automatic method to create flow lines for determination of glacier length: A pilot study with Alaskan glaciers, *Computers & Geosciences*, 52, 234-245.

LEMMENS, M. (2017) The Fierce Rise of Airborne Lidar: a view on status, developments and trends, *GIM International*, **31**(1), 16-19.

LI, K., LI, H., WANG, L., GAO, W. (2011) On the Relationship between Local Topography and Small Glacier Change under Climatic Warming on Mt. Bogda, Eastern Tian Shan, China, *Journal of Earth Science*, **22**(4), 515-527.

LIU, X., ZHANG, Z., PETERSON, J., CHANDRA, S. (2007) The effect of LiDAR data density on DEM accuracy, *Proceedings of International congress on modelling and simulation (MODSIM07)*, Christchurch, New Zealand, 1363-1369.

MASINI, N., COLUZZI, R., LASAPONARA, R. (2011) On the Airborne Lidar Contribution in Archaeology: from Site Identification to Landscape Investigation, in: Wang, C.C. (ed.) Laser Scanning, Theory and Applications, Intech, 263–290.

MAUNE, D.F. (2007) Digital elevation model technologies and applications: The DEM User's Manual, 2nd ed., Bethesda: American Society for Photogrammetry and Remote Sensing.

MCCULLAGH, M. (1988) Terrain and surface modeling systems: theory and practice, *Photogrammetric Record*, 12, 747–779.

MENNIS, J.L., FOUNTAIN, A.G. (2001) A spatio-temporal GIS database for monitoring alpine glacier change, *Photogrammetric Engineering and Remote Sensing*, **67**(8), 967–975.

MOORE, I.D., GRAYSON, R.B., LADSON, A.R. (1991) Digital Terrain Modelling: A Review of Hydrological, Geomorphological and Biological Applications, *Hydrological Processes*, 5, 3-30.

MOREIRA, A., PRATS-IRAOLA, P., YOUNIS, M., KRIEGER, G., HAJNSEK, I., PAPATHANASSIOU, K.P. (2013) A Tutorial on Synthetic Aperture Radar, *IEEE Geoscience and Remote Sensing Magazine*, **1**(1), 6-43.

MUKHERJEE, S., JOSHI, P.K., MUKHERJEE, S., GHOSH, A., GARG, R.D., MUKHOPADHYAY, A. (2013) Evaluation of vertical accuracy of open source Digital Elevation Model (DEM), *International Journal of Applied Earth Observation and Geoinformation*, 21, 205-217.

NAEGELI, K., DAMM, A., HUSS, M., WULF, H., SCHAEPMAN, M., HOELZLE, M. (2017) Cross-Comparison of Albedo Products for Glacier Surfaces Derived from Airborne and Satellite (Sentinel-2 and Landsat 8) Optical Data, *Remote Sensing*, **9**(110), 1-22.

NEELMEIJER, J., MOTAGH, M., BOOKHAGEN, B. (2017) High-resolution digital elevation models from single-pass TanDEM-X interferometry over mountainous regions: A case study of Inylchek Glacier, Central Asia, *ISPRS Journal of Photogrammetry and Remote Sensing*, 130, 108-121.

NUTH, C., KÄÄB, A. (2011) Co-registration and bias corrections of satellite elevation data sets for quantifying glacier thickness change, *The Cryosphere*, 5, 271–290.

PAUL, F., KÄÄB, A., MAISCH, M., KELLENBERGER, T., HAEBERLI, W. (2002) The new remote- sensing-derived Swiss glacier inventory: I. methods, *Annals of Glaciology*, 34, 355–361.

PEPE, A., CALÒ, F. (2017) A Review of Interferometric Synthetic Aperture RADAR (InSAR) Multi-Track Approaches for the Retrieval of Earth's Surface Displacements, *Applied Sciences*, **7**(1264), 1-39.

QUATTROCHI, D.A., GOODCHILD, M.F., (eds.) (1997) Scale in remote sensing and GIS, Boca Raton: CRC Press.

QUINCEY, D.J., BISHOP, M.P., KÄÄB, A., BERTHIER, E., FLACH, B., BOLCH, T., BUCHROITHNER, M., KAMP, U., KHALSA, S.J.S., TOUTIN, T., HARITASHYA, U.K., RACOVITEANU, A., SHRODER, J.F., RAUP, B.H. (2014) Digital terrain modeling and glacier topographic characterization, in: Kargel, J.S., Leonard, G.J., Bishop, M.P., Kääb, A., Raup, B.H. (eds.) Global Land Ice Measurements from Space, Heidelberg: Springer Verlag, pp. 113-145.

RABATEL, A., SIRGUEY, P., DROLON, V., MAISONGRANDE, P., ARNAUD, Y., BERTHIER, E., DAVAZE, L., DEDIEU, J.P., DUMONT, M. (2017), Annual and Seasonal Glacier-Wide Surface Mass Balance Quantified from Changes in Glacier Surface State: A Review on Existing Methods Using Optical Satellite Imagery, *Remote Sensing*, **9**(507), 1-22.

RACOVITEANU, A.E., MANLEY, W.F., ARNOUD, Y, WILLIAMS, M.W. (2007) Evaluating digital elevation models for glaciologic applications: An example from Nevado Coropuna, Peruvian Andes, *Global and Planetary Change*, 59, 110-125.

RAMACHANDRAN, B., DWYER, J., RAUP, B.H., KARGEL, J.S. (2014) ASTER datasets and derived products for global glacier monitoring, in: Kargel, J.S., Leonard, G.J., Bishop, M.P., Kääb, A., Raup, B.H. (eds.) Global Land Ice Measurements from Space, Heidelberg: Springer Verlag, pp. 145-162.

REES, W.G., ARNOLD, N.S. (2006) Scale-dependent roughness of a glacier surface: implications for radar backscatter and aerodynamic roughness modelling, *Journal of Glaciology*, **52**(177), 214-222.

RICHARDS, J.A. (2009) Remote Sensing with Imaging Radar, Heidelberg: Springer Verlag.

RIVERA, A., BENHAM, T., CASASSA, G., BAMBER, J., DOWDESWELL, J.A. (2007) Ice elevation and areal changes of glaciers from the Northern Patagonia Icefield, Chile, *Global and Planetary Change*, 59, 126-137.

RIZZOLI, P., BRÄUTIGAM, B., KRAUS, T., MARTONE, M., KRIEGER, G. (2012) Relative height error analysis of TanDEM-X elevation data, *ISPRS Journal of Photogrammetry and Remote Sensing*, 73, 30-38.

SAILER, R., GEIST, T., STÖTTER, J., STRASSER, U. (2017) Hintereisferner (Ötztal, Tyrol, Austria) Digital Elevation Models (1 x 1 m) from Airborne Laser Scanning Data Set 2001-2013, in supplement to Strasser, U., Marke, T., Braun, L.N., Escher-Vetter, H., Juen, I., Kuhn, M., Maussion, F., Mayer, C., Nicholson, L., Niedertscheider, K., Sailer, R., Stötter, J., Weber, M., Kaser, G. (2018) The Rofental: a high Alpine research basin (1890–3770 ma.s.l.) in the Ötztal Alps (Austria) with over 150 years of hydrometeorological and glaciological observations, *Earth System Science Data*, 10, 151-171.

SCHELLENBERGER, T., VAN WYCHEN, W., COPLAND, L., KÄÄB, A., GRAY, L. (2016) An Inter-Comparison of Techniques for Determining Velocities of Maritime Arctic Glaciers, Svalbard, Using Radarsat-2 Wide Fine Mode Data, *Remote Sensing*, **8**(785), 1-16.

SCHERLER, D., BOOKHAGEN, B., STRECKER, M.R. (2011) Hillslope-glacier coupling: The interplay of topography and glacial dynamics in High Asia, *Journal of Geophysical* Research, 116, F02019.

SEVESTRE, H., BENN, D.I. (2015) Climatic and geometric controls on the global distribution of surge-type glaciers: implications for a unifying model of surging, *Journal of Glaciology*, **61**(228), 646-662.

SHAN, J. & TOTH, C.K. (2008) Topographic Laser Ranging and Scanning: Principles and Processing, Boca Raton: CRC Press.

SHI, W.Z.J., LI, Z.L., BEDARD, Y. (2004) Theme issue: advanced techniques for analysis of geo-spatial data, *ISPRS Journal of Photogrammetry and Remote Sensing*, 59, 1–5.

STRASSER, U., MARKE, T., BRAUN, L.N., ESCHER-VETTER, H., JUEN, I., KUHN, M., MAUSSION, F., MAYER, C., NICHOLSON, L., NIEDERTSCHEIDER, K., SAILER, R., STÖTTER, J., WEBER, M., KASER, G. (2018) The Rofental: a high Alpine research basin (1890–3770 ma.s.l.) in the Ötztal Alps (Austria) with over 150 years of hydrometeorological and glaciological observations, *Earth System Science Data*, 10, 151-171.

TACHIKAWA, T., KAKU, M., IWASAKI, A., GESCH, D., OIMOEN, M., ZHANG, Z., DANIELSON, J., KRIEGER, T., CURTIS, B., HAASE, J., ABRAMS, M., CRIPPEN, R., CARABAJAL, C. (2011) *ASTER Global Digital Elevation Model Version 2 – Summary of Validation Results*, Joint Japan–US ASTER Science Team (METI & NASA).

TANG, J., PILESJÖ, P., PERSSON, A. (2013) Estimating slope from raster data – a test of eight algorithms at different resolutions in flat and steep terrain, *Geodesy and Cartography*, **39**(2), 41-52.

TELLING, J.W., GLENNIE, C., FOUNTAIN, A.G., FINNEGAN, D.C. (2017) Analyzing Glacier Surface Motion Using LiDAR Data, *Remote Sensing*, **9**(283), 1-12.

TOBLER, W.R. (1970) A Computer Movie Simulating Urban Growth in the Detroit Region, *Economic Geography*, 46, 234-240.

VAZE, J., TENG, J., SPENCER, G. (2010) Impact of DEM accuracy and resolution on topographic indices, *Environmental modelling & Software*, 25, 1086-1098.

VIJAY, S., BRAUN, M.H. (2016) Elevation Change Rates of Glaciers in the Lahaul-Spiti (Western Himalaya, India) during 2000–2012 and 2012–2013, *Remote Sensing*, **8**(1038), 1-16.

VOSSELMAN, G. & MAAS, H.G. (2010) Airborne and Terrestrial Laser Scanning, Dunbeath: Whittles Publishing.

WECHSLER, S.P., KROLL, C.N. (2006) Quantifying DEM Uncertainty and its Effect on Topographic Parameters, *Photogrammetric Engineering & Remote Sensing*, **72**(9), 1081-1090.

WENG, Q. (2002) Quantifying uncertainty of digital elevation models derived from topographic maps, in: Richardson, D.E., Van Oosterom, O., (eds.) Advances in spatial data handling: 10th International Symposium on Spatial Data Handling, Berlin: Springer, 403–418.

YAMAGUCHI, Y., KAHLE, A.B., TSU, H., KAWAKAMI, T., PNIEL, M. (1998) Overview of advanced spaceborne thermal emission and reflection radiometer (ASTER), *IEEE Transactions on Geoscience and Remote Sensing*, **36**(4), 1062–1071.

Series from Lund University

Department of Physical Geography and Ecosystem Science

Master Thesis in Geographical Information Science

1. *Anthony Lawther:* The application of GIS-based binary logistic regression for slope failure susceptibility mapping in the Western Grampian Mountains, Scotland (2008).
2. *Rickard Hansen:* Daily mobility in Grenoble Metropolitan Region, France. Applied GIS methods in time geographical research (2008).
3. *Emil Bayramov:* Environmental monitoring of bio-restoration activities using GIS and Remote Sensing (2009).
4. *Rafael Villarreal Pacheco:* Applications of Geographic Information Systems as an analytical and visualization tool for mass real estate valuation: a case study of Fontibon District, Bogota, Columbia (2009).
5. *Siri Oestreich Waage:* a case study of route solving for oversized transport: The use of GIS functionalities in transport of transformers, as part of maintaining a reliable power infrastructure (2010).
6. *Edgar Pimiento:* Shallow landslide susceptibility – Modelling and validation (2010).
7. *Martina Schäfer:* Near real-time mapping of floodwater mosquito breeding sites using aerial photographs (2010).
8. *August Pieter van Waarden-Nagel:* Land use evaluation to assess the outcome of the programme of rehabilitation measures for the river Rhine in the Netherlands (2010).
9. *Samira Muhammad:* Development and implementation of air quality data mart for Ontario, Canada: A case study of air quality in Ontario using OLAP tool. (2010).
10. *Fredros Oketch Okumu*: Using remotely sensed data to explore spatial and temporal relationships between photosynthetic productivity of vegetation and malaria transmission intensities in selected parts of Africa (2011).
11. *Svajunas Plunge:* Advanced decision support methods for solving diffuse water pollution problems (2011).
12. *Jonathan Higgins:* Monitoring urban growth in greater Lagos: A case study using GIS to monitor the urban growth of Lagos 1990 - 2008 and produce future growth prospects for the city (2011).
13. *Mårten Karlberg:* Mobile Map Client API: Design and Implementation for Android (2011).
14. *Jeanette McBride:* Mapping Chicago area urban tree canopy using color infrared imagery (2011).
15. *Andrew Farina:* Exploring the relationship between land surface temperature and vegetation abundance for urban heat island mitigation in Seville, Spain (2011).
16. *David Kanyari*: Nairobi City Journey Planner: An online and a Mobile Application (2011).

17. *Laura V. Drews:* Multi-criteria GIS analysis for siting of small wind power plants - A case study from Berlin (2012).
18. *Qaisar Nadeem:* Best living neighborhood in the city - A GIS based multi criteria evaluation of ArRiyadh City (2012).
19. *Ahmed Mohamed El Saeid Mustafa:* Development of a photo voltaic building rooftop integration analysis tool for GIS for Dokki District, Cairo, Egypt (2012).
20. *Daniel Patrick Taylor*: Eastern Oyster Aquaculture: Estuarine Remediation via Site Suitability and Spatially Explicit Carrying Capacity Modeling in Virginia's Chesapeake Bay (2013).
21. *Angeleta Oveta Wilson:* A Participatory GIS approach to *unearthing* Manchester's Cultural Heritage '*gold mine'* (2013).
22. *Ola Svensson:* Visibility and Tholos Tombs in the Messenian Landscape: A Comparative Case Study of the Pylian Hinterlands and the Soulima Valley (2013).
23. *Monika Ogden:* Land use impact on water quality in two river systems in South Africa (2013).
24. *Stefan Rova:* A GIS based approach assessing phosphorus load impact on Lake Flaten in Salem, Sweden (2013).
25. *Yann Buhot:* Analysis of the history of landscape changes over a period of 200 years. How can we predict past landscape pattern scenario and the impact on habitat diversity? (2013).
26. *Christina Fotiou:* Evaluating habitat suitability and spectral heterogeneity models to predict weed species presence (2014).
27. *Inese Linuza:* Accuracy Assessment in Glacier Change Analysis (2014).
28. *Agnieszka Griffin:* Domestic energy consumption and social living standards: a GIS analysis within the Greater London Authority area (2014).
29. *Brynja Guðmundsdóttir:* Detection of potential arable land with remote sensing and GIS - A Case Study for Kjósarhreppur (2014).
30. *Oleksandr Nekrasov:* Processing of MODIS Vegetation Indices for analysis of agricultural droughts in the southern Ukraine between the years 2000-2012 (2014).
31. *Sarah Tressel:* Recommendations for a polar Earth science portal in the context of Arctic Spatial Data Infrastructure (2014).
32. *Caroline Gevaert:* Combining Hyperspectral UAV and Multispectral Formosat-2 Imagery for Precision Agriculture Applications (2014).
33. *Salem Jamal-Uddeen:* Using GeoTools to implement the multi-criteria evaluation analysis - weighted linear combination model (2014).
34. *Samanah Seyedi-Shandiz:* Schematic representation of geographical railway network at the Swedish Transport Administration (2014).
35. *Kazi Masel Ullah:* Urban Land-use planning using Geographical Information System and analytical hierarchy process: case study Dhaka City (2014).
36. *Alexia Chang-Wailing Spitteler:* Development of a web application based on MCDA and GIS for the decision support of river and floodplain rehabilitation projects (2014).
37. *Alessandro De Martino:* Geographic accessibility analysis and evaluation of potential changes to the public transportation system in the City of Milan (2014).
38. *Alireza Mollasalehi:* GIS Based Modelling for Fuel Reduction Using Controlled Burn in Australia. Case Study: Logan City, QLD (2015).

39. *Negin A. Sanati:* Chronic Kidney Disease Mortality in Costa Rica; Geographical Distribution, Spatial Analysis and Non-traditional Risk Factors (2015).
40. *Karen McIntyre:* Benthic mapping of the Bluefields Bay fish sanctuary, Jamaica (2015).
41. *Kees van Duijvendijk:* Feasibility of a low-cost weather sensor network for agricultural purposes: A preliminary assessment (2015).
42. *Sebastian Andersson Hylander:* Evaluation of cultural ecosystem services using GIS (2015).
43. *Deborah Bowyer:* Measuring Urban Growth, Urban Form and Accessibility as Indicators of Urban Sprawl in Hamilton, New Zealand (2015).
44. *Stefan Arvidsson:* Relationship between tree species composition and phenology extracted from satellite data in Swedish forests (2015).
45. *Damián Giménez Cruz*: GIS-based optimal localisation of beekeeping in rural Kenya (2016).
46. *Alejandra Narváez Vallejo:* Can the introduction of the topographic indices in LPJ-GUESS improve the spatial representation of environmental variables? (2016).
47. *Anna Lundgren:* Development of a method for mapping the highest coastline in Sweden using breaklines extracted from high resolution digital elevation models (2016).
48. *Oluwatomi Esther Adejoro:* Does location also matter? A spatial analysis of social achievements of young South Australians (2016).
49. *Hristo Dobrev Tomov:* Automated temporal NDVI analysis over the Middle East for the period 1982 - 2010 (2016).
50. *Vincent Muller:* Impact of Security Context on Mobile Clinic Activities A GIS Multi Criteria Evaluation based on an MSF Humanitarian Mission in Cameroon (2016).
51. *Gezahagn Negash Seboka:* Spatial Assessment of NDVI as an Indicator of Desertification in Ethiopia using Remote Sensing and GIS (2016).
52. *Holly Buhler:* Evaluation of Interfacility Medical Transport Journey Times in Southeastern British Columbia. (2016).
53. *Lars Ole Grottenberg*: Assessing the ability to share spatial data between emergency management organisations in the High North (2016).
54. *Sean Grant:* The Right Tree in the Right Place: Using GIS to Maximize the Net Benefits from Urban Forests (2016).
55. *Irshad Jamal:* Multi-Criteria GIS Analysis for School Site Selection in Gorno-Badakhshan Autonomous Oblast, Tajikistan (2016).
56. *Fulgencio Sanmartín:* Wisdom-volkano: A novel tool based on open GIS and time-series visualization to analyse and share volcanic data (2016).
57. *Nezha Acil:* Remote sensing-based monitoring of snow cover dynamics and its influence on vegetation growth in the Middle Atlas Mountains (2016).
58. *Julia Hjalmarsson:* A Weighty Issue: Estimation of Fire Size with Geographically Weighted Logistic Regression (2016).
59. *Mathewos Tamiru Amato:* Using multi-criteria evaluation and GIS for chronic food and nutrition insecurity indicators analysis in Ethiopia (2016).
60. *Karim Alaa El Din Mohamed Soliman El Attar:* Bicycling Suitability in Downtown, Cairo, Egypt (2016).

61. *Gilbert Akol Echelai:* Asset Management: Integrating GIS as a Decision Support Tool in Meter Management in National Water and Sewerage Corporation (2016).
62. *Terje Slinning:* Analytic comparison of multibeam echo soundings (2016).
63. *Gréta Hlín Sveinsdóttir:* GIS-based MCDA for decision support: A framework for wind farm siting in Iceland (2017).
64. *Jonas Sjögren:* Consequences of a flood in Kristianstad, Sweden: A GIS-based analysis of impacts on important societal functions (2017).
65. *Nadine Raska:* 3D geologic subsurface modelling within the Mackenzie Plain, Northwest Territories, Canada (2017).
66. *Panagiotis Symeonidis*: Study of spatial and temporal variation of atmospheric optical parameters and their relation with PM 2.5 concentration over Europe using GIS technologies (2017).
67. *Michaela Bobeck:* A GIS-based Multi-Criteria Decision Analysis of Wind Farm Site Suitability in New South Wales, Australia, from a Sustainable Development Perspective (2017).
68. *Raghdaa Eissa*: Developing a GIS Model for the Assessment of Outdoor Recreational Facilities in New Cities Case Study: Tenth of Ramadan City, Egypt (2017).
69. *Zahra Khais Shahid*: Biofuel plantations and isoprene emissions in Svea and Götaland (2017).
70. *Mirza Amir Liaquat Baig*: Using geographical information systems in epidemiology: Mapping and analyzing occurrence of diarrhea in urban - residential area of Islamabad, Pakistan (2017).
71. *Joakim Jörwall*: Quantitative model of Present and Future well-being in the EU-28: A spatial Multi-Criteria Evaluation of socioeconomic and climatic comfort factors (2017).
72. *Elin Haettner*: Energy Poverty in the Dublin Region: Modelling Geographies of Risk (2017).
73. *Harry Eriksson*: Geochemistry of stream plants and its statistical relations to soil- and bedrock geology, slope directions and till geochemistry. A GIS-analysis of small catchments in northern Sweden (2017).
74. *Daniel Gardevärn:* PPGIS and Public meetings – An evaluation of public participation methods for urban planning (2017).
75. *Kim Friberg:* Sensitivity Analysis and Calibration of Multi Energy Balance Land Surface Model Parameters (2017).
76. *Viktor Svanerud:* Taking the bus to the park? A study of accessibility to green areas in Gothenburg through different modes of transport (2017).
77. *Lisa-Gaye Greene*: Deadly Designs: The Impact of Road Design on Road Crash Patterns along Jamaica's North Coast Highway (2017).
78. *Katarina Jemec Parker*: Spatial and temporal analysis of fecal indicator bacteria concentrations in beach water in San Diego, California (2017).
79. *Angela Kabiru*: An Exploratory Study of Middle Stone Age and Later Stone Age Site Locations in Kenya's Central Rift Valley Using Landscape Analysis: A GIS Approach (2017).
80. *Kristean Björkmann*: Subjective Well-Being and Environment: A GIS-Based Analysis (2018).
81. *Williams Erhunmonmen Ojo*: Measuring spatial accessibility to healthcare for people living with HIV-AIDS in southern Nigeria (2018).

82. *Daniel Assefa*: Developing Data Extraction and Dynamic Data Visualization (Styling) Modules for Web GIS Risk Assessment System (WGRAS). (2018).
83. *Adela Nistora*: Inundation scenarios in a changing climate: assessing potential impacts of sea-level rise on the coast of South-East England (2018).
84. *Marc Seliger*: Thirsty landscapes - Investigating growing irrigation water consumption and potential conservation measures within Utah's largest master-planned community: Daybreak (2018).
85. *Luka Jovičić*: Spatial Data Harmonisation in Regional Context in Accordance with INSPIRE Implementing Rules (2018).
86. *Christina Kourdounouli*: Analysis of Urban Ecosystem Condition Indicators for the Large Urban Zones and City Cores in EU (2018).
87. *Jeremy Azzopardi*: Effect of distance measures and feature representations on distance-based accessibility measures (2018).
88. *Patrick Kabatha*: An open source web GIS tool for analysis and visualization of elephant GPS telemetry data, alongside environmental and anthropogenic variables (2018).
89. *Richard Alphonce Giliba*: Effects of Climate Change on Potential Geographical Distribution of Prunus africana (African cherry) in the Eastern Arc Mountain Forests of Tanzania (2018).
90. *Eiður Kristinn Eiðsson*: Transformation and linking of authoritative multi-scale geodata for the Semantic Web: A case study of Swedish national building data sets (2018).
91. *Niamh Harty*: HOP!: a PGIS and citizen science approach to monitoring the condition of upland paths (2018).
92. *José Estuardo Jara Alvear*: Solar photovoltaic potential to complement hydropower in Ecuador: A GIS-based framework of analysis (2018).
93. *Brendan O'Neill*: Multicriteria Site Suitability for Algal Biofuel Production Facilities (2018).
94. *Roman Spataru*: Spatial-temporal GIS analysis in public health – a case study of polio disease (2018).
95. *Alicja Miodońska*: Assessing evolution of ice caps in Suðurland, Iceland, in years 1986 - 2014, using multispectral satellite imagery (2019).
96. *Dennis Lindell Schettini*: A Spatial Analysis of Homicide Crime's Distribution and Association with Deprivation in Stockholm Between 2010-2017 (2019).
97. *Damiano Vesentini*: The Po Delta Biosphere Reserve: Management challenges and priorities deriving from anthropogenic pressure and sea level rise (2019).
98. *Emilie Arnesten*: Impacts of future sea level rise and high water on roads, railways and environmental objects: a GIS analysis of the potential effects of increasing sea levels and highest projected high water in Scania, Sweden (2019).
99. *Syed Muhammad Amir Raza*: Comparison of geospatial support in RDF stores: Evaluation for ICOS Carbon Portal metadata (2019).
100. *Hemin Tofiq*: Investigating the accuracy of Digital Elevation Models from UAV images in areas with low contrast: A sandy beach as a case study (2019).
101. *Evangelos Vafeiadis*: Exploring the distribution of accessibility by public transport using spatial analysis. A case study for retail concentrations and public hospitals in Athens (2019).
102. *Milan Sekulic*: Multi-Criteria GIS modelling for optimal alignment of roadway by-passes in the Tlokweng Planning Area, Botswana (2019).

103. *Ingrid Piirisaar*: A multi-criteria GIS analysis for siting of utility-scale photovoltaic solar plants in county Kilkenny, Ireland (2019).
104. *Nigel Fox*: Plant phenology and climate change: possible effect on the onset of various wild plant species' first flowering day in the UK (2019).
105. *Gunnar Hesch*: Linking conflict events and cropland development in Afghanistan, 2001 to 2011, using MODIS land cover data and Uppsala Conflict Data Programme (2019).
106. *Elijah Njoku*: Analysis of spatial-temporal pattern of Land Surface Temperature (LST) due to NDVI and elevation in Ilorin, Nigeria (2019).
107. *Katalin Bunyevácz*: Development of a GIS methodology to evaluate informal urban green areas for inclusion in a community governance program (2019).
108. *Paul dos Santos*: Automating synthetic trip data generation for an agent-based simulation of urban mobility (2019).
109. *Robert O' Dwyer*: Land cover changes in Southern Sweden from the mid-Holocene to present day: Insights for ecosystem service assessments (2019).
110. *Daniel Klingmyr*: Global scale patterns and trends in tropospheric NO2 concentrations (2019).
111. *Marwa Farouk Elkabbany*: Sea Level Rise Vulnerability Assessment for Abu Dhabi, United Arab Emirates (2019).
112. *Jip Jan van Zoonen*: Aspects of Error Quantification and Evaluation in Digital Elevation Models for Glacier Surfaces (2020).